



MOX-Report No. 29/2020

**Modeling cardiac muscle fibers in ventricular and
atrial electrophysiology simulations**

Piersanti, R.; Africa, P.C.; Fedele, M.; Vergara, C.; Dede', L.;
Corno, A.F.; Quarteroni, A.

MOX, Dipartimento di Matematica
Politecnico di Milano, Via Bonardi 9 - 20133 Milano (Italy)

mox-dmat@polimi.it

<http://mox.polimi.it>

Modeling cardiac muscle fibers in ventricular and atrial electrophysiology simulations

Roberto Piersanti^a, Pasquale C. Africa^a, Marco Fedele^a, Christian Vergara^b, Luca Dedè^a, Antonio F. Corno^c, and Alfio Quarteroni^{a,d}

^aModellistica e Calcolo Scientifico (MOX), Dipartimento di Matematica, Politecnico di Milano, Milan, Italy

^bLaboratory of Biological Structure Mechanics (LaBS), Dipartimento di Chimica, Materiali e Ingegneria Chimica, Politecnico di Milano, Milan, Italy

^cEast Midlands Congenital Heart Center, University Hospitals of Leicester, University of Leicester, Glenfield Hospital, Leicester, United Kingdom

^dInstitute of Mathematics, École Polytechnique Fédérale de Lausanne, Switzerland (Professor emeritus)

May 8, 2020

Keywords: Cardiac fiber architecture; Fiber reconstruction; Laplace-Dirichlet-Rule-Based-Methods; Mathematical models; Electrophysiology simulation; Finite element method.

Abstract

Since myocardial fibers drive the electric signal propagation throughout the myocardium, accurately modeling their arrangement is essential for simulating heart electrophysiology (EP). Rule-Based-Methods (RBMs) represent a commonly used strategy to include cardiac fibers in computational models. A particular class of such methods is known as Laplace-Dirichlet-Rule-Based-Methods (LDRBMs) since they rely on the solution of Laplace problems. In this work we provide a unified framework, based on LDRBMs, for generating full heart muscle fibers. We first present a unified description for existing ventricular LDRBMs, introducing some modeling improvements with respect to the existing literature. We then carry out a systematic comparison of LDRBMs based on meaningful biomarkers produced by numerical EP simulations. Next we propose, for the first time, a LDRBM to be used for generating atrial fibers. The new method, tested both on idealized and realistic atrial models, can be applied to any arbitrary geometries. Finally, we present numerical results obtained in a realistic whole heart where fibers are included for all the four chambers using the discussed LDRBMs.

1 Introduction

In numerical heart electrophysiology a critical issue is that of modeling the myocardial fibers arrangement that characterizes the cardiac tissue. Aggregations of myofibers, namely the results of cardiomyocytes orientation, determine how the electric signal propagates within the muscle [1, 2, 3]. This motivates the need to accurately include fiber orientations in order to obtain physically meaningful results [4, 5].

In the last decades, myofibers orientation have been studied using histological data and Diffusion Tensor Imaging (DTI) acquisition [6, 7, 8]. DTI is a Magnetic Resonance Imaging (MRI) technique able to produce useful structural information about heart muscle fibers and largely applied to explanted ex-vivo hearts, coming from animal experiments [6, 7, 9, 10, 11] or from human corpses [8, 12]. However, acquired in-vivo DTI protocol lasts hours and generally produces a noisy low-resolution fibers reconstruction [13, 14, 15]. Furthermore, since the atria thickness is smaller than the DTI voxel size, it is not possible to obtain in-vivo myofibers in the atria [16]. All the above considerations make nowadays DTI technique unusable to reconstruct accurate 3D myofibers field in the common clinical practice.

Because of the difficulties to acquire patient-specific fibers data, different methodologies have been proposed in order to provide a realistic surrogate of fiber orientation for in-vivo cardiac geometries [12, 16, 17, 18, 19, 20, 21, 22, 23]. Among these, atlas-based methods map and project a detailed fiber field, previously reconstructed on an atlas, on the geometry of interest, exploiting DTI or histological data; see [12] for the ventricles and [16] for the atria. However, these methods require complex registration algorithms and are strictly dependent on the original atlas data upon which they have been built.

Alternative strategies for generating myofiber orientations are the so called *Rule-Based Methods* (RBMs) [4, 24, 25, 26]. RBMs describe fiber orientations with mathematically sound rules based on histological or DTI observations and require information only about the myocardial geometry. These methods parametrize the transmural and apico-basal directions in the entire myocardium in order to assign orthotropic (longitudinal, transversal and normal) myofibers; see [5, 17, 18, 19, 20, 24] for the ventricles and [21, 22, 23, 27, 28] for the atria.

A particular class of RBMs, which rely on the solution of Laplace boundary-value problems, is known as *Laplace-Dirichlet-Rule-Based-Methods* (LDRBMs), addressed in [5, 17, 18, 19, 20] for the ventricular case. LDRBMs define the transmural and apico-basal directions by taking the gradient of solutions corresponding to suitable Dirichlet boundary conditions. These directions are then properly rotated in order to match histological observations [29, 30, 31]. The above procedure ensures a smooth and continuous change in fibers directions throughout the whole myocardium.

Most of existing ventricular RBMs refer to left ventricle only and usually introduce an artificial basal plane located well below the cardiac valves. Only

recently, a LDRBM, that takes into account fiber directions in specific cardiac regions, such as the right ventricle, the inter-ventricular septum and the outflow tracks, has been developed [20]. This has provided a great improvement in RBMs since the right ventricle exhibits a different fiber orientation with respect to the left ventricle [7, 9, 12, 32]. The presence of a discontinuity in the inter-ventricular septal fibers is a crucial matter, still very debated [32, 33], even though the corresponding effects on electrical signal propagation have not been studied yet.

Regarding the atria, several RBMs have been developed. They either use semi-automatic approaches [21, 22, 23, 27, 28, 34, 35, 36] or prescribe manually the fiber orientations in specific atrial regions [37, 38, 39, 40]. Often, these procedures require a manual intervention and, in many cases, are designed for specific atrial morphologies [21, 23]. Hence, a general automatic processing pipeline for generating atrial fibers field still remains a knotty procedure [23, 41]. Moreover, no LDRBMs have been proposed so far for the atria. As a matter of fact, an extension of the ventricular LDRBMs is not straightforward, mainly because the atrial fibers architecture is characterized by the presence of multiple overlapping bundles running along different directions, differently from the ventricles one where myofibers are aligned along regular patterns.

Over the past years several cardiac computational models were carried out in order to study pathological conditions affecting either the electrical or mechanical response in individual heart chambers. However, in the quest for a more quantitative understanding of the heart functioning both in health and diseased scenarios, it became fundamental to model and simulate the entire heart as an whole organ [42]. Only recently, the scientific community moved towards the whole heart modeling and simulations [43, 44, 45, 46, 47, 48, 49, 50]. Nevertheless, we highlight that none of these computational studies makes use of a unified methodology to embed reliable and detailed cardiac fibers in the whole heart muscle to take into account different fiber orientations specific of the four chambers.

Driven by the previous open issues, in this work we provide a unified framework, based on LDRBMs, for generating full heart muscle fibers. We start by giving a unified mathematical description for three existing LDRBMs in the ventricles, introducing also some modeling improvements [17, 19, 20]. In particular, we extend ventricular LDRBMs in order to include specific fiber directions for the right ventricle. Next, we carry out a systematic comparison of the effect produced by different LDRBMs on the electrophysiology in terms of meaningful biomarkers (e.g. activation times) computed from numerical simulations. Specifically, we study the importance of including different fiber orientations in the right ventricle and we investigate the effect of the inter-ventricular septal fibers discontinuity.

Then, at the best of our knowledge, we propose for the first time an atrial LDRBM which is able to qualitatively reproduce all the important features, such as fiber bundles, needed to provide a realistic atrial musculature architecture.

Unlike most of the existing RBMs, the new method, tested both on idealized and realistic atrial geometries, can be easily applied to any arbitrary geometries. Moreover, we analyse the strong effect of the complex atrial fiber architecture on the electric signal propagation obtained by numerical simulations.

In the last part of the work, we illustrate numerical results including the full heart LDRBMs fiber generations and an electrophysiology simulation with physiological activation sites in a four chamber realistic computational domain of the heart.

This paper is organized as follows. In Section 2 we review and provide a unified description of existing LDRBMs for ventricular fiber generation. In Section 3 we propose our new LDRBM for atrial fibers generation. Numerical methods to perform electrophysiology simulations are explained in Section 4. Section 5 is dedicated to numerical results where we present a comparison among different ventricular LDRBMs, we test by means of electrophysiological simulations the new atrial LDRBM and we show numerical simulation of the whole heart electrophysiology including the presented fiber generation methods. Finally, conclusions follow.

2 Rule-Based-Methods for ventricular fibers generation

In this section we review three popular LDRBMs introduced so far in the literature: specifically, we consider LDRBMs by Rossi et al. [19], by Bayer et al. [17] and by Doste et al. [20]. In view of our review process of the former LDRBMs, we provide a unified framework of such methods, highlighting commonalities and differences.

We identify the following shared steps of the three ventricular LDRBMs ¹, which are hereby reported:

1. **Labelled mesh:** Provide a labelled mesh of the ventricles domain Ω_{myo} to define specific partitions of the ventricles boundary $\partial\Omega_{myo}$, see Figure 1;
2. **Transmural distance:** A *transmural distance* is defined to compute the distance of the epicardium from endocardium surfaces;
3. **Transmural direction:** The transmural distance gradient is used to build the unit *transmural direction* \hat{e}_t of the ventricles, see Figure 1;
4. **Normal direction:** An apico-basal direction (directed from the apex towards the ventricles base) is introduced and it is used to build the unit *normal direction* \hat{e}_n , orthogonal to the transmural one, see Figure 1;

¹In what follows, we consider the three LDRBMs applied to biventricular models, the most general case of ventricles domain.

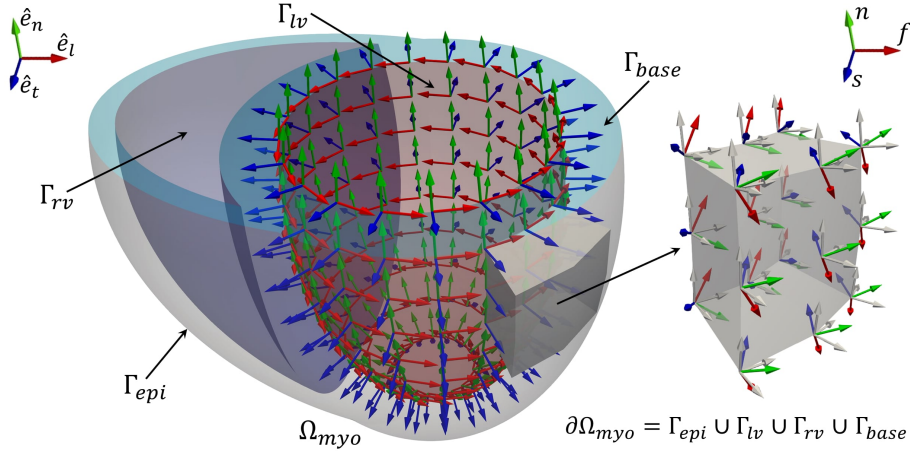


Figure 1: Left: Representation of the three directions employed by a LDRBM for an idealized biventricular domain Ω_{myo} whose border $\partial\Omega_{myo}$ is partitioned in the epicardium Γ_{epi} , left Γ_{lv} and right Γ_{rv} endocardium and the ventricles base Γ_{base} , $\partial\Omega_{myo} = \Gamma_{epi} \cup \Gamma_{lv} \cup \Gamma_{rv} \cup \Gamma_{base}$. For visualization purpose, only directions on the left endocardium Γ_{lv} are represented. In blue: unit transmural direction, \hat{e}_t ; In green: unit normal direction, \hat{e}_n ; In red: unit longitudinal direction, \hat{e}_l . Right: zoom on a slab of the left ventricle myocardium Ω_{myo} showing the three final myofibers orientations \mathbf{f} , \mathbf{s} , \mathbf{n} .

5. **Local coordinate system:** Build for each point of the ventricles domain an orthonormal local coordinate axial system composed by \hat{e}_t , \hat{e}_n and the unit *longitudinal direction* \hat{e}_l (orthogonal to the previous ones), see Figure 1;
6. **Rotate axis:** Finally, properly rotate the reference frame with the purpose of defining the myofiber orientations: \mathbf{f} the *fiber direction*, \mathbf{n} the *cross-fiber direction* and \mathbf{s} the *sheet direction*, see Figure 1(right). Rotations are chosen in order to match histology and DTI observations.

The ventricular LDRBM by Rossi et al [19, 46] (in what follows referred to as R-RBM) is a modified version of the algorithm studied in [18] for generating fibers in left ventricular geometries [19], then extended to the biventricular case in [46]. R-RBM is based on the definition of the transmural direction. Bayer et al. [17] developed another LDRBM (B-RBM) for assigning myocardial fiber orientation introducing two major contributions. The first improvement is the definition of the apico-basal direction [5]. The second one consists of using the bi-direction spherical interpolation (*bislerp*) [51, 52] to manage the fiber orientations in order to guarantee a smooth and continuous change in the fiber field, particularly in the proximity of the septum and around the ventricle junctions [17]. Both R-RBM and B-RBM introduce an artificial basal plane, located well below the cardiac valves, delimiting the ventricle regions. To overcome this restriction,

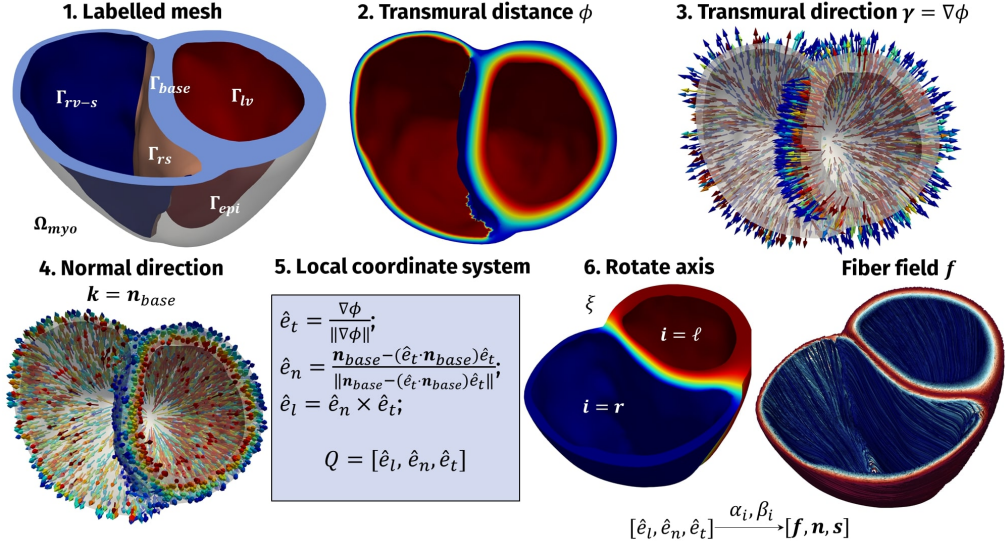


Figure 2: Schematic pipeline of R-RBM for a biventricular geometry with an artificial basal plane.

Doste et al. [20] recently proposed a new LDRBM (D-RBM) which is able to build the fiber field in a full biventricular geometry without the need to cut it with a basal plane. D-RBM fiber orientations are generated to take into account specific ventricular regions, such as the inter-ventricular septum and outflow tracts (OT), following observations from histological studies [20].

To characterize the three LDRBMs under review, it is useful to consider the following Laplace-Dirichlet problem

$$\begin{cases} -\Delta\chi = 0 & \text{in } \Omega_{myo}, \\ \chi = \chi_a & \text{on } \Gamma_a, \\ \chi = \chi_b & \text{on } \Gamma_b, \\ \nabla\chi \cdot \mathbf{n} = 0 & \text{on } \Gamma_n, \end{cases} \quad (1)$$

for a generic unknown χ and suitable boundary data $\chi_a, \chi_b \in \mathbb{R}$ set on generic partitions of the ventricles boundary $\Gamma_a, \Gamma_b, \Gamma_n$, with $\Gamma_a \cup \Gamma_b \cup \Gamma_n = \partial\Omega_{myo}$. The variable χ will assume different meanings depending on the step and LDRBM considered. Moreover, the values χ_a, χ_b are fixed in order to evaluate specific inter-ventricular distances between boundary partitions Γ_a, Γ_b .

We detail in what follows the six points aforementioned. We refer to Figures 2, 3 and 4, showing a schematic representations of R-RBM, B-RBM, and D-RBM, respectively, for a biventricular domain Ω_{myo} .

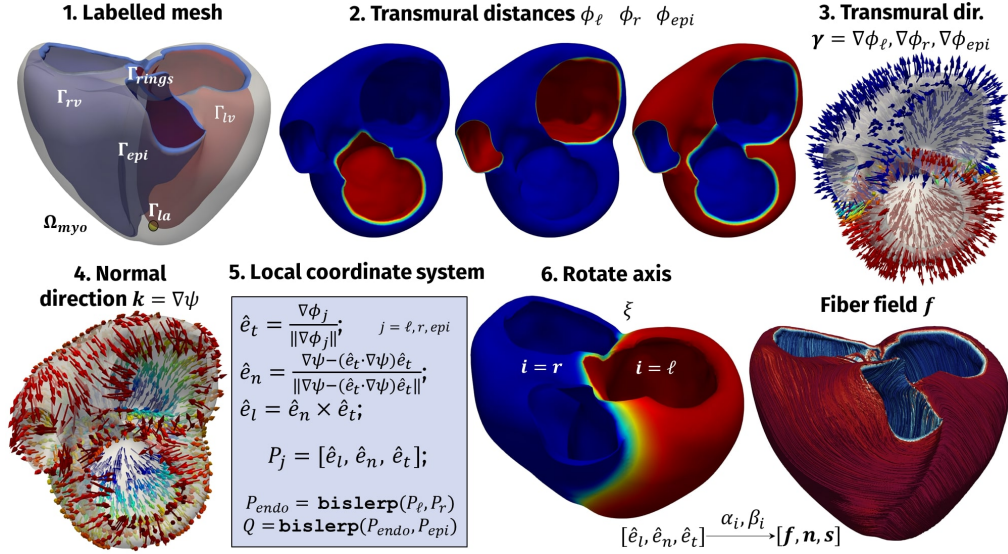


Figure 3: Schematic pipeline of B-RBM for a full biventricular geometry.

1. Labelled mesh Prescribing the ventricles boundary $\partial\Omega_{myo}$. All the three LDRBMs define the following boundaries:

Γ_{epi} : the ventricles epicardium, Γ_{base} : the ventricles base,
 Γ_{lv} : the left ventricle endocardium, Γ_{rv} : the right ventricle endocardium.

Moreover, R-RBM subdivides the right ventricle endocardium Γ_{rv} into the right ventricle septum Γ_{rs} and the remaining part Γ_{rv-s} such that $\Gamma_{rv} = \Gamma_{rs} \cup \Gamma_{rv-s}$, see step 1 in Figure 2. This subdivision is usually performed manually by the user, thus introducing some arbitrariness during the septum selection. For B-RBM and D-RBM the left ventricle apex Γ_{la} is also introduced, whereas the right ventricle apex Γ_{ra} for D-RBM solely (see step 1 in Figures 3 and 4). Furthermore, D-RBM requires boundary tags for the four valve rings: Γ_{mv} (mitral valve), Γ_{av} (aortic valve), Γ_{tv} (tricuspid valve) and Γ_{pv} (pulmonary valve), see step 1 in Figure 4. It is also useful to define $\Gamma_{rings} = \Gamma_{lring} \cup \Gamma_{rring}$, with $\Gamma_{lring} = \Gamma_{mv} \cup \Gamma_{av}$ and $\Gamma_{rring} = \Gamma_{tv} \cup \Gamma_{pv}$. Notice that in B-RBM we considered the union of the four valve rings as the ventricles base $\Gamma_{base} = \Gamma_{rings}$. This allows the use of B-RBM also in the case of a full biventricular geometry, see step 1 in Figure 3. In summary, the three methods define the boundary $\partial\Omega_{myo}$ as follows (see step 1 in Figures 2, 3 and 4):

$$\text{R-RBM} : \partial\Omega_{myo} = \Gamma_{epi} \cup \Gamma_{lv} \cup \Gamma_{rs} \cup \Gamma_{rv-s} \cup \Gamma_{base},$$

$$\text{B-RBM} : \partial\Omega_{myo} = \Gamma_{epi} \cup \Gamma_{lv} \cup \Gamma_{rv} \cup \Gamma_{rings} \cup \Gamma_{la},$$

$$\text{D-RBM} : \partial\Omega_{myo} = \Gamma_{epi} \cup \Gamma_{lv} \cup \Gamma_{rv} \cup \Gamma_{mv} \cup \Gamma_{av} \cup \Gamma_{tv} \cup \Gamma_{pv} \cup \Gamma_{la} \cup \Gamma_{ra}.$$

LDRBM type	Transmural distances	χ_a	Γ_a	χ_b	Γ_b	Γ_n
R-RBM	ϕ	1	$\Gamma_{lv} \cup \Gamma_{rv-s}$	0	$\Gamma_{epi} \cup \Gamma_{rs}$	Γ_{base}
B-RBM	ϕ_ℓ	1	Γ_{lv}	0	$\Gamma_{epi} \cup \Gamma_{rv}$	Γ_{rings}
	ϕ_r	1	Γ_{rv}	0	$\Gamma_{epi} \cup \Gamma_{lv}$	Γ_{rings}
	ϕ_{epi}	1	Γ_{epi}	0	$\Gamma_{lv} \cup \Gamma_{rv}$	Γ_{rings}
D-RBM	ϕ	2	Γ_{lv}	0	Γ_{epi}	Γ_{rings}
		-1	Γ_{rv}			

Table 1: Transmural distance boundary conditions for R-RBM, B-RBM and D-RBM used in step 2.

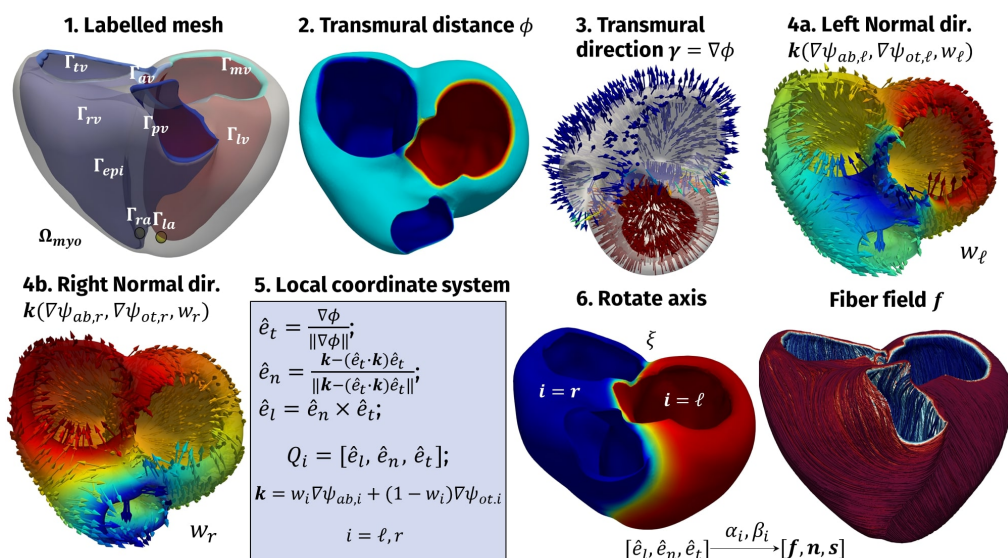


Figure 4: Schematic pipeline of D-RBM for a full biventricular geometry.

2. Transmural distance Definition of transmural distances (generally indicated with the letter ϕ) obtained by solving Laplace-Dirichlet problems of the form (1). In particular, for R-RBM, the transmural distance ϕ is found by solving (1) with $\chi_a = 1$ on $\Gamma_{lv} \cup \Gamma_{rv-s}$, $\chi_b = 0$ on $\Gamma_{epi} \cup \Gamma_{rs}$, and $\Gamma_n = \Gamma_{base}$. For D-RBM, ϕ is found by solving (1) with $\chi_a = 2$ on Γ_{lv} , $\chi_a = -1$ on Γ_{rv} , $\chi_b = 0$ on Γ_{epi} , and $\Gamma_n = \Gamma_{rings}$. B-RBM requires to solve three Laplace problems (1) in order to compute three different transmural distances ϕ_ℓ , ϕ_r and ϕ_{epi} . We refer the reader to Table 1 for the specific choices in problem (1) made by the three methods. Notice that in D-RBM the boundary conditions χ_a are assigned in order to identify the two ventricles (positive and negative values for left and right ventricle, respectively) and to associate roughly two-thirds of the septum to the left ventricle and one-third to the right one [20] (see step 2 in Figures 2, 3 and 4).

3. Transmural direction After solving the Laplace problems for finding the transmural distances ϕ , ϕ_l , ϕ_r , ϕ_{epi} , their gradients define the transmural directions γ (see step 3 in Figures 2, 3 and 4). In particular, we have:

$$\begin{aligned} \text{R-RBM} : \gamma &= \nabla\phi, \\ \text{B-RBM} : \gamma &= \nabla\phi_i, \quad i = \ell, r, epi, \\ \text{D-RBM} : \gamma &= \nabla\phi. \end{aligned}$$

4. Normal direction Definition of the normal direction \mathbf{k} . In R-RBM, this is done using the vector \mathbf{n}_{base} , i.e. the outward normal to the ventricular base, that is $\mathbf{k} = \mathbf{n}_{base}$ (see step 4 in Figure 2). For the other two LDRBMs, further variables (identified by the letter ψ) are introduced: they are found by solving the Laplace problem in the form (1) with suitable boundary conditions. Specifically, for B-RBM the vector \mathbf{k} is the gradient of the solution ψ ($\mathbf{k} = \nabla\psi$) obtained with $\chi_a = 1$ on Γ_{rings} , $\chi_b = 0$ on Γ_{la} , and $\Gamma_n = \Gamma_{epi} \cup \Gamma_{lv} \cup \Gamma_{rv}$, see step 4 in Figure 3. In D-RBM, instead, two normal directions are introduced, one for each ventricle:

$$\mathbf{k} = w_i \nabla\psi_{ab,i} + (1 - w_i) \nabla\psi_{ot,i}, \quad i = \ell, r, \quad (2)$$

where $i = \ell, r$ refer to the left and right ventricle, respectively, so that the normal direction is a weighted sum of apico-basal ($\nabla\psi_{ab,i}$) and apico-outflow-tract ($\nabla\psi_{ot,i}$) directions, obtained using an inter-ventricular interpolation function w_i [20]; the latter are given again by solutions of problems like (1) (see step 4a and 4b in Figure 4). In particular, $\psi_{ab,\ell}$, $\psi_{ab,r}$, $\psi_{ot,\ell}$, $\psi_{ot,r}$, w_ℓ , w_r are found by solving (1) with $\chi_a = 1$ on Γ_a and $\chi_b = 0$ on Γ_b , where Γ_a and Γ_b are boundary subsets listed in Table 2. Summing up, the different methods compute the normal direction \mathbf{k} as follows (see step 4 in Figures 2, 3 and 4):

$$\begin{aligned} \text{R-RBM} : \mathbf{k} &= \mathbf{n}_{base}, \\ \text{B-RBM} : \mathbf{k} &= \nabla\psi, \\ \text{D-RBM} : \mathbf{k} &= w_i \nabla\psi_{ab,i} + (1 - w_i) \nabla\psi_{ot,i}, \quad i = \ell, r. \end{aligned}$$

5. Local coordinate system Building an orthonormal local coordinate system (defined by letter Q) at each point of the domain Ω_{myo} . All the three methods make use of the following function **axis**:

$$P = [\hat{\mathbf{e}}_\ell, \hat{\mathbf{e}}_n, \hat{\mathbf{e}}_t] = \mathbf{axis}(\mathbf{k}, \gamma) = \begin{cases} \hat{\mathbf{e}}_t &= \frac{\gamma}{\|\gamma\|}, \\ \hat{\mathbf{e}}_n &= \frac{\mathbf{k} - (\mathbf{k} \cdot \hat{\mathbf{e}}_t) \hat{\mathbf{e}}_t}{\|\mathbf{k} - (\mathbf{k} \cdot \hat{\mathbf{e}}_t) \hat{\mathbf{e}}_t\|}, \\ \hat{\mathbf{e}}_\ell &= \hat{\mathbf{e}}_n \times \hat{\mathbf{e}}_t, \end{cases} \quad (3)$$

which takes as input a normal direction \mathbf{k} and a transmural direction γ and returns the orthonormal system P whose columns are the three orthonormal directions $\hat{\mathbf{e}}_\ell$, $\hat{\mathbf{e}}_n$, $\hat{\mathbf{e}}_t$ which represent the longitudinal, the normal and the transmural

Scalar potentials	Γ_a	Γ_b	Γ_n
$\psi_{ab,\ell}$	Γ_{mv}	Γ_{la}	$\Gamma_{epi} \cup \Gamma_{lv} \cup \Gamma_{rv} \cup \Gamma_{av} \cup \Gamma_{rring}$
$\psi_{ab,r}$	Γ_{tv}	Γ_{ra}	$\Gamma_{epi} \cup \Gamma_{lv} \cup \Gamma_{rv} \cup \Gamma_{pv} \cup \Gamma_{lring}$
$\psi_{ot,\ell}$	Γ_{av}	Γ_{la}	$\Gamma_{epi} \cup \Gamma_{lv} \cup \Gamma_{rv} \cup \Gamma_{mv} \cup \Gamma_{rring}$
$\psi_{ot,r}$	Γ_{pv}	Γ_{ra}	$\Gamma_{epi} \cup \Gamma_{lv} \cup \Gamma_{rv} \cup \Gamma_{tv} \cup \Gamma_{lring}$
w_ℓ	$\Gamma_{mv} \cup \Gamma_{la}$	Γ_{av}	$\Gamma_{epi} \cup \Gamma_{lv} \cup \Gamma_{rv} \cup \Gamma_{rring}$
w_r	$\Gamma_{tv} \cup \Gamma_{ra}$	Γ_{pv}	$\Gamma_{epi} \cup \Gamma_{lv} \cup \Gamma_{rv} \cup \Gamma_{lring}$

Table 2: Scalar potentials used in D-RBM to build the normal direction.

unit directions, respectively. For R-RBM we have $Q = \mathbf{axis}(\mathbf{k}, \nabla\phi)$. For B-RBM three orthonormal coordinate systems are introduced, that is $P_\ell = \mathbf{axis}(\mathbf{k}, \nabla\phi_\ell)$, $P_r = \mathbf{axis}(\mathbf{k}, \nabla\phi_r)$ and $P_{epi} = \mathbf{axis}(\mathbf{k}, \nabla\phi_{epi})$, which are then interpolated through the function `bislerp` to obtain a continuous orthonormal coordinate system within the whole myocardium (see [17] for further details). Hence, B-RBM performs the following steps to obtain the final orthonormal coordinate system Q (see step 5 in Figure 3):

$$\begin{aligned} P_{endo} &= \mathbf{bislerp}(P_\ell, P_r), \\ Q &= \mathbf{bislerp}(P_{endo}, P_{epi}). \end{aligned}$$

D-RBM, instead, defines two different coordinate systems for left and right ventricle as a consequence of the normal directions defined in (2) (see step 5 in Figure 4):

$$Q_i = \mathbf{axis}(w_i \nabla\psi_{ab,i} + (1 - w_i) \nabla\psi_{ot,i}, \nabla\phi), \quad i = \ell, r.$$

6. Rotate axis The orthonormal coordinate system, defined for each point of the myocardium at the previous step, should be aligned in order to match histological knowledge about fiber and sheet orientations. To this aim, the three LDRBMs introduce a rotation of $\hat{\mathbf{e}}_\ell, \hat{\mathbf{e}}_n, \hat{\mathbf{e}}_t$ by means of suitable angles: the longitudinal direction $\hat{\mathbf{e}}_\ell$ rotates counter-clockwise around $\hat{\mathbf{e}}_t$ by an angle α_i , whereas the transmural direction $\hat{\mathbf{e}}_t$ is rotated counter-clockwise around $\hat{\mathbf{e}}_\ell$ by an angle β_i , where $i = \ell, r$ depend on the left or right ventricle the point belongs to. Indeed, it is known that in the left and right ventricles the fiber orientations feature a change in direction at the inter-ventricular septum [32]. In order to obtain a local orthonormal coordinate system, direction $\hat{\mathbf{e}}_n$ is rotated accordingly.

These rotations produce a map from the original coordinate system to a new coordinate system $[\mathbf{f}, \mathbf{n}, \mathbf{s}]$:

$$[\hat{\mathbf{e}}_\ell, \hat{\mathbf{e}}_n, \hat{\mathbf{e}}_t] \xrightarrow{\alpha_i, \beta_i} [\mathbf{f}, \mathbf{n}, \mathbf{s}], \quad i = \ell, r,$$

where \mathbf{f} is the fiber direction, \mathbf{n} is the cross-fiber direction and \mathbf{s} is the sheet direction.

For all the three methods the rotation angles $\alpha_i = \alpha_i(d_i)$ and $\beta_i = \beta_i(d_i)$ are functions of the position within the myocardium, in particular of the *transmural normalized distance* $d_i \in [0, 1]$, $i = \ell, r$, defined as:

$$\begin{aligned} \text{R-RBM} : d_\ell = d_r = \phi, \\ \text{B-RBM} : d_\ell = \phi_\ell \quad d_r = \phi_r, \\ \text{D-RBM} : d_\ell = \phi/2 \quad d_r = |\phi|. \end{aligned}$$

Accordingly, the rotation angles are written by means of the following linear relationships:

$$\alpha_i(d_i) = \alpha_{epi,i}(1 - d_i) + \alpha_{endo,i}d_i, \quad \beta_i(d_i) = \beta_{epi,i}(1 - d_i) + \beta_{endo,i}d_i, \quad i = \ell, r, \quad (4)$$

where $\alpha_{endo,\ell}$, $\alpha_{epi,\ell}$, $\alpha_{endo,r}$, $\alpha_{epi,r}$, $\beta_{endo,\ell}$, $\beta_{epi,\ell}$, $\beta_{endo,r}$ and $\beta_{epi,r}$ are suitable rotation angles on the epicardium and endocardium chosen in order to match histological observations. For example, classical values found in the literature are $\alpha_{epi,\ell} = +60^\circ$, $\alpha_{endo,\ell} = -60^\circ$, $\alpha_{epi,r} = -25^\circ$, $\alpha_{endo,r} = +90^\circ$ [12, 29, 31, 53, 54].

In order to differentiate between the left and right ventricles and to apply the correct angles, we propose here to use the solution of an additional Laplace problem (1) in the unknown $\chi = \xi$ with $\chi_a = 1$ on Γ_{lv} , $\chi_b = -1$ on Γ_{rv} , and $\Gamma_n = \Gamma_{base} \cup \Gamma_{epi}$ ². In particular, positive values of ξ identify the left ventricle, whereas negative values the right one [55]. This new feature enables to perform different rotations for left and right ventricles (see steps 6 in Figures 2, 3 and 4) that is crucial in order to generate realistic fiber fields. An alternative method has been proposed in [20] but only for D-RBM. It is worth mentioning that the original R-RBM [19, 46] introduces a rotation to obtain the fiber field \mathbf{f} only. Here we propose an extension in order to define also \mathbf{n} and \mathbf{s} .

Further, B-RBM exploits two other functions representing the rotation angles within the septum:

$$\alpha_s(d_i) = \alpha_{endo,i}(1 - 2d_i), \quad \beta_s(d_i) = \beta_{endo,i}(1 - 2d_i), \quad i = \ell, r,$$

whereas with similar expressions, D-RBM introduces also the possibility to set specific fiber and sheet angles rotation in the OT regions (see [17] and [20] for further details).

We conclude pointing out that B-RBM and D-RBM can be applied to the full biventricular geometry and to the based biventricular case (that is obtained with an artificial basal plane well below the cardiac valves). Indeed, in the based biventricular geometry the whole procedure for B-RBM and D-RBM remains the same as long as the ring tags are replaced by the base tag, $\Gamma_{rings} = \Gamma_{base}$. On the contrary, R-RBM is less suitable for a full biventricular case because it is not able to strictly identify the normal direction \mathbf{k} as the outward normal to the ventricular rings. Besides, the definition of right ventricle septum Γ_{rs} can be arbitrary for a full biventricular geometry.

²Let us observe that, for B-RBM $\Gamma_{base} = \Gamma_{rings}$ in the case of a full biventricular geometry. Moreover, for D-RBM solely $\chi_a = 2$ in order to be compliant with the transmural distance.

3 A new rule-based method for atrial fibers generation

Atrial fibers architecture is very different from that of the ventricles where myofibers are aligned in a regular pattern [1]. Indeed, fibers in the atria are organized in individual bundles running along different directions throughout the wall chambers. Preferred orientation of myofibers in the human atria is characterized by multiple overlapping structures, which promote the formation of separate attached bundles [56]. This architecture has a strong influence in the electric signal propagation inside the atrial muscle [21, 27, 57, 58, 59, 60, 61].

Over the past years many histological studies investigated the fibers arrangement of the atria revealing a very complex texture musculature [62, 63, 64, 65, 66, 67, 68, 69]. Nevertheless, there is a paucity of imaging data on atrial fibers orientation with respect to the ventricles, mainly due to imaging difficulties in capturing the thin atrial walls [56]. Only recently, *ex vivo* atrial fibers have been analysed owing to submillimeter *Diffusion Tensor MRI* imaging [8, 70, 71].

In computational models of cardiac electrophysiology, atrial fiber orientations have been generated in specific regions either manually [37, 38, 39, 40] or using a variety of semi-automatic rule-based approaches [21, 22, 23, 27, 28, 34, 35, 36]. Recently, atlas-based methods, in which fiber directions of a reference atrial geometry are warped on a target geometry, have been introduced [16, 72, 73, 74]. All the former procedures require manual intervention introducing, for example, various distinct landmarks, seed-points and a network of auxiliaries lines [21, 23]. Hence, a processing pipeline for generating atrial fibers field still remains a knotty procedure [23, 41].

In this section we propose for the first time a LDRBM for the generation of atrial myofibers, which is able to qualitatively reproduce all the important features, such as fiber bundles, needed to provide a realistic atrial musculature architecture. Our newly developed method is inspired by [74] where Laplace problems are introduced to map variables between two geometries and by LDRBMs, purposely built for the ventricles, presented in Section 2 [17, 19, 20]. The extension of the latter is not straightforward due to the presence of bundles which run in different directions. For this reason, our atrial LDRBM combines the gradient of several harmonic functions to represent the fiber bundles.

In what follows we detail the four steps of the proposed atrial LDRBM. We refer to Figure 5 for a schematic representation of the method in a realistic scenario.

1. Labelled mesh Label the mesh of the atrial computational domain Ω_{atrial} to define the boundary partitions of $\partial\Omega_{atrial}$. For both the left atrium (LA) and the right atrium (RA) the following boundaries are defined (see step 1 in Figure

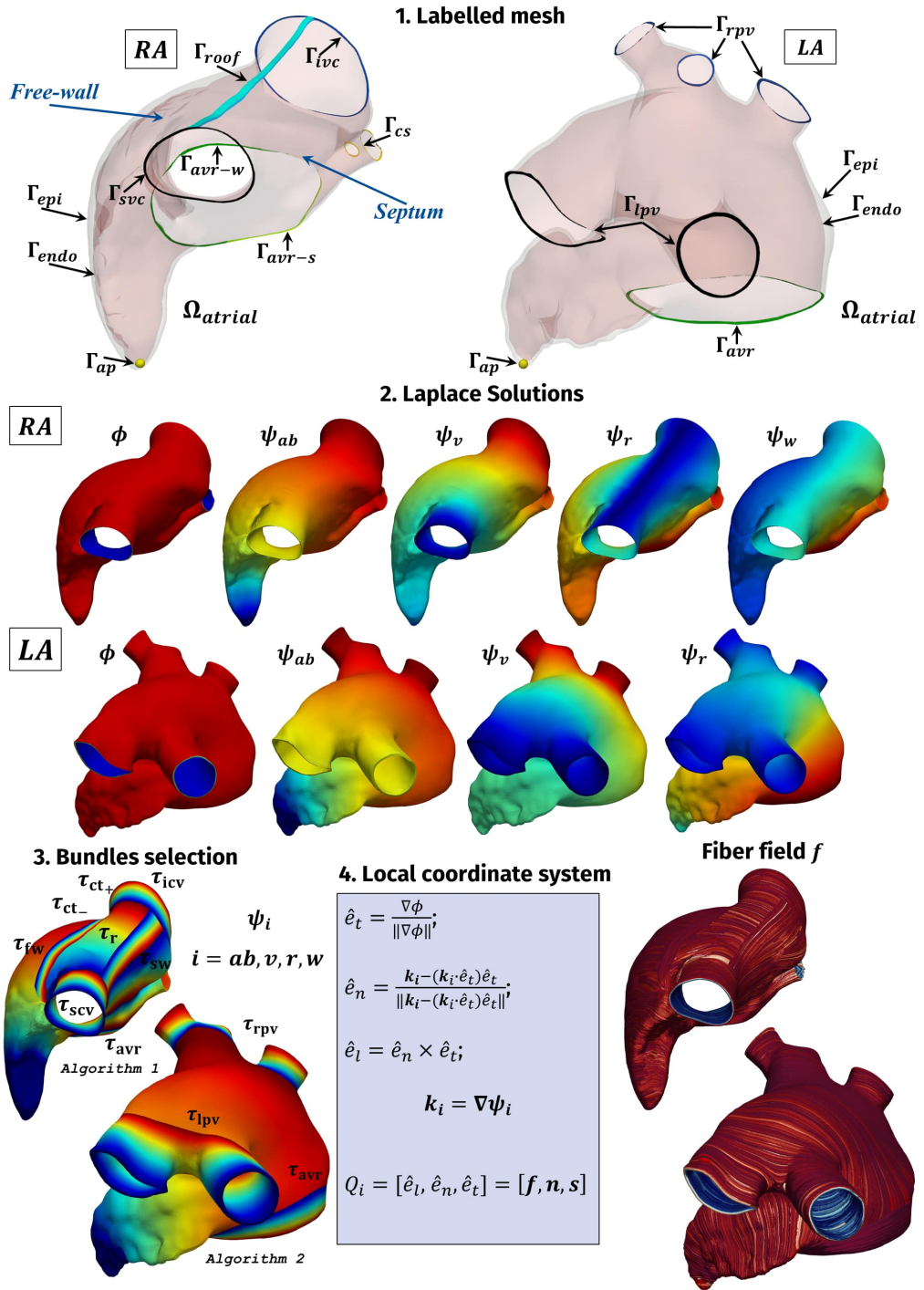


Figure 5: Schematic pipeline of the atrial LDRBM in a realistic right atrium (RA) and left atrium (LA) geometries.

Type	χ	χ_a	Γ_a	χ_b	Γ_b	Γ_n
LA	ϕ	1	Γ_{epi}	0	Γ_{endo}	$\Gamma_{avr} \cup \Gamma_{lpv} \cup \Gamma_{rpv}$
	ψ_{ab}	2	Γ_{rpv}	1	Γ_{avr}	$\Gamma_{epi} \cup \Gamma_{endo}$
		0	Γ_{lpv}	-1	Γ_{ap}	
	ψ_v	1	Γ_{rpv}	0	Γ_{lpv}	$\Gamma_{avr} \cup \Gamma_{epi} \cup \Gamma_{endo}$
	ψ_r	1	Γ_{avr}	0	$\Gamma_{lpv} \cup \Gamma_{rpv} \cup \Gamma_{ap}$	$\Gamma_{epi} \cup \Gamma_{endo}$
RA	ϕ	1	$\Gamma_{epi} \cup \Gamma_{r-epi}$	0	$\Gamma_{endo} \cup \Gamma_{r-endo}$	$\Gamma_{avr} \cup \Gamma_{icv} \cup \Gamma_{scv} \cup \Gamma_{cs}$
	ψ_{ab}	2	Γ_{icv}	1	Γ_{avr}	$\Gamma_{epi} \cup \Gamma_{endo} \cup \Gamma_{roof} \cup \Gamma_{cs}$
		0	Γ_{scv}	-1	Γ_{ap}	
	ψ_v	1	Γ_{icv}	0	$\Gamma_{scv} \cup \Gamma_{ap}$	$\Gamma_{avr} \cup \Gamma_{epi} \cup \Gamma_{endo} \cup \Gamma_{roof} \cup \Gamma_{cs}$
	ψ_r	1	Γ_{avr}	0	Γ_{roof}	$\Gamma_{epi} \cup \Gamma_{endo} \cup \Gamma_{icv} \cup \Gamma_{scv} \cup \Gamma_{cs}$
	ψ_w	1	Γ_{avr-s}	-1	Γ_{avr-w}	$\Gamma_{epi} \cup \Gamma_{endo} \cup \Gamma_{roof} \cup \Gamma_{icv} \cup \Gamma_{scv} \cup \Gamma_{cs}$

Table 3: Boundary data chosen in the Laplace problem (1) for the transmural distance ϕ and the inter-atrial distances ψ_i ($i = ab, v, r, w$) in the left (LA) and right atrium (RA).

5):

$$\begin{aligned} \Gamma_{endo} &: \text{the atrium endocardium,} & \Gamma_{epi} &: \text{the atrium epicardium,} \\ \Gamma_{avr} &: \text{the atrio-ventricular ring,} & \Gamma_{ap} &: \text{the atrium appendage.} \end{aligned}$$

Moreover, we introduce boundary tags of the left and right pulmonary vein rings Γ_{lpv} , Γ_{rpv} for the LA, and the tags of the inferior and superior caval vein rings Γ_{icv} , Γ_{scv} and of the coronary sinus ring Γ_{cs} for the RA. In the RA, the atrio-ventricular ring Γ_{avr} is equally subdivided in one part facing the atrial septum Γ_{avr-s} and another one related to the free wall Γ_{avr-w} , such that $\Gamma_{avr} = \Gamma_{avr-s} \cup \Gamma_{avr-w}$ (see step 1 in Figure 5). Furthermore, the RA encloses also the boundary tag for the atrial roof Γ_{roof} that is divided in two sections: a part lying on the epicardium $\Gamma_{roof-epi}$ and another one on the endocardium $\Gamma_{roof-endo}$, such that $\Gamma_{roof} = \Gamma_{roof-epi} \cup \Gamma_{roof-endo}$ (see step 1 in Figure 5). In summary, the boundaries $\partial\Omega_{atrial}$ for the RA and LA are, respectively:

$$\begin{aligned} \text{RA} : \partial\Omega_{atrial} &= \Gamma_{epi} \cup \Gamma_{endo} \cup \Gamma_{ap} \cup \Gamma_{icv} \cup \Gamma_{scv} \cup \Gamma_{cs} \cup \Gamma_{avr-s} \cup \Gamma_{avr-w} \cup \\ &\quad \cup \Gamma_{roof-epi} \cup \Gamma_{roof-endo}; \\ \text{LA} : \partial\Omega_{atrial} &= \Gamma_{epi} \cup \Gamma_{endo} \cup \Gamma_{ap} \cup \Gamma_{lpv} \cup \Gamma_{rpv} \cup \Gamma_{avr}. \end{aligned}$$

2. Laplace solutions Definition of the transmural distance ϕ and several inter-atrial distances ψ_i , obtained by solving a Laplace-Dirichlet problem in the form of (1) with proper Dirichlet boundary conditions on the atrial boundaries, see step 2 in Figure 5. Refer to Table 3 for the specific choices in problem (1) made for the RA and LA. In particular, ψ_{ab} is the solution of a Laplace problem (1) with three different boundary data prescribed on the atrio-ventricular ring Γ_{avr} , the atrial appendage Γ_{ap} , and the rings of the caval veins for the RA and the pulmonary veins for the LA; ψ_v represents the distance between the caval veins for the RA and among the pulmonary veins for the LA; ψ_r stands for the distance between the atrio-ventricular ring Γ_{avr} and the roof Γ_{roof} (RA)

Algorithm 1 Bundles selection for right atrium in the atrial LDRBM

Let τ_{avr} , τ_r , τ_{icv} , τ_{scv} , τ_{ct+} , τ_{ct-} , τ_{fw} , and τ_{sw} be the parameters referring to the bundles dimension.

```
if  $\psi_r \geq \tau_{avr}$  set  $\mathbf{k} = \nabla\psi_r$ 
else
  if  $\psi_r < \tau_r$ 
    if  $\psi_w \geq \tau_{ct-}$  and  $\psi_w \leq \tau_{ct+}$  set  $\mathbf{k} = \nabla\psi_w$ 
    else if  $\psi_w < \tau_{ct-}$ 
      if  $\psi_v \geq \tau_{icv}$  or  $\psi_v \leq \tau_{scv}$  set  $\mathbf{k} = \nabla\psi_v$ 
      else set  $\mathbf{k} = \nabla\psi_{ab}$ 
    else
      if  $\psi_v \geq \tau_{icv}$  or  $\psi_v \leq \tau_{scv}$  set  $\mathbf{k} = \nabla\psi_v$ 
      else
        if  $\psi_w \leq \tau_{fw}$  set  $\mathbf{k} = \nabla\psi_v$ 
        else if  $\psi_w \geq \tau_{sw}$  set  $\mathbf{k} = \nabla\psi_r$ 
        else set  $\mathbf{k} = \nabla\psi_w$ 
  else
    if  $\psi_v \geq \tau_{icv}$  or  $\psi_v \leq \tau_{scv}$  set  $\mathbf{k} = \nabla\psi_v$ 
    else
      if  $\psi_w \geq 0$  set  $\mathbf{k} = \nabla\psi_r$ 
      else set  $\mathbf{k} = \nabla\psi_{ab}$ 
```

Algorithm 2 Bundles selection for left atrium in the atrial LDRBM

Let τ_{avr} , τ_{lpv} and τ_{rpv} be the parameters referring to the bundles dimension.

```
if  $\psi_r \geq \tau_{avr}$  set  $\mathbf{k} = \nabla\psi_r$ 
else
  if  $\psi_v \geq \tau_{lpv}$  or  $\psi_v \leq \tau_{rpv}$  set  $\mathbf{k} = \nabla\psi_v$ 
  else set  $\mathbf{k} = \nabla\psi_{ab}$ 
```

and between Γ_{avr} and the union of the pulmonary veins rings $\Gamma_{lpv} \cup \Gamma_{rpv}$ (LA). Moreover, for the RA ψ_w is the distance between the atrioventricular ring of the free (Γ_{avr-w}) and the septum (Γ_{avr-s}) walls. See step 2 in Figure 5.

3. Bundles selection Definition of the atrial bundles and their dimension throughout the domain Ω_{atrial} , in order to match histology and DTI observations. With this aim, the atrial LDRBM assigns, for each point in Ω_{atrial} , a unique inter-atrial distance ψ_i , among those defined in step 2, following the rules reported in Algorithms 1 and 2 for the bundle selection in the right and left atrium, respectively (see also step 3 in Figure 5). During this assignment, the atrial LDRBM defines a unique normal direction \mathbf{k} by taking the gradient of the allocated inter-atrial distances, $\mathbf{k} = \nabla\psi_i$. Moreover, in order to specify the bundles dimension, the parameters τ_i are introduced: for the RA τ_{avr} , τ_r ,

τ_{icv} , τ_{scv} , τ_{ct+} , τ_{ct-} , τ_{fw} and τ_{sw} referring to the atrio-ventricular, roof, inferior and superior caval veins, crista terminalis, free and septum wall bundles, respectively; for the LA τ_{avr} , τ_{lpv} and τ_{rpv} referring to the atrio-ventricular, left and right pulmonary veins bundles, respectively. The complete bundles selection procedures are displayed in details in Algorithms 1 and 2 (see also step 3 in Figure 5).

4. Local coordinate system Definition of the myofiber orientations by means of an orthonormal local coordinate system, built at each point of the atrial domain. This step is performed in the same way as for the ventricles: the gradient of the transmural distance ϕ is used to build the transmural direction $\nabla\phi$ which is taken as one input of the function `axis` (3) together with the unique normal direction \mathbf{k} :

$$Q = [\hat{\mathbf{e}}_l, \hat{\mathbf{e}}_n, \hat{\mathbf{e}}_t] = [\mathbf{f}, \mathbf{n}, \mathbf{s}] = \text{axis}(\mathbf{k}, \nabla\phi),$$

where $\hat{\mathbf{e}}_l$, $\hat{\mathbf{e}}_n$ and $\hat{\mathbf{e}}_t$ are the unit longitudinal, normal and transmural directions, respectively. Moreover, since we are not prescribing any transmural variation in the fiber bundles, the three unit directions correspond to the final fiber, sheet and cross-fiber directions \mathbf{f} , \mathbf{n} and \mathbf{s} (see step 4 in Figure 5).

4 Modelling cardiac electrophysiology

In this section we briefly recall the mathematical model for the description of the electrophysiology activity in the cardiac tissue, that is the monodomain equation [75, 76] endowed with suitable ionic models for human action potential, i.e the *Courtemanche-Ramirez-Nattel* model for the atria [77] and the *Ten-Tusscher-Panfilov* model for the ventricles [78]. Moreover, we provide the corresponding methods used for the numerical approximation (Section 4.2).

4.1 Mathematical models

Front propagation of cardiac action potential can be simulated by the monodomain model: a reaction-diffusion partial differential equation describing current flow through cardiac tissue, composed of myocytes that are electrically connected via a low-resistance gap junctions, coupled with an ionic model described by a system of ordinary differential and algebraic equations standing for ionic exchange across cell membranes [46, 56, 75, 79, 80, 81, 82].

Cardiac tissue is an orthotropic material, arising from the cellular organization of the myocardium in fibers, laminar sheet and cross-fibers, which is mathematically modelled by the conductivity tensor

$$\mathbb{D} = \sigma_f \mathbf{f} \otimes \mathbf{f} + \sigma_s \mathbf{s} \otimes \mathbf{s} + \sigma_n \mathbf{n} \otimes \mathbf{n}, \quad (5)$$

where σ_f , σ_s and σ_n are the conductivities along fibers (\mathbf{f}), sheets (\mathbf{s}), and cross-fibers (\mathbf{n}) directions, respectively. Given a computational domain Ω and a time interval $(0, T]$, the monodomain equations read:

find, for each t , the transmembrane action potential $u : \Omega \times (0, T] \rightarrow \mathbb{R}$ and the gating variables $\mathbf{w} : \Omega \times (0, T] \rightarrow \mathbb{R}^n$, such that

$$\chi C_m \frac{\partial u}{\partial t} - \nabla \cdot (\mathbb{D} \nabla u) + \chi I_{ion}(u, \mathbf{w}) = I_{app}(\mathbf{x}, t) \quad \text{in } \Omega \times (0, T], \quad (6a)$$

$$\frac{d\mathbf{w}}{dt} = \mathbf{G}(u, \mathbf{w}) \quad \text{in } \Omega \times (0, T], \quad (6b)$$

where χ is the surface area-to-volume ratio of cardiomyocytes, C_m is the specific trans-membrane capacitance per unit area, I_{app} is an external applied current which serves to initiate the signal propagation, I_{ion} and $\mathbf{G} \in \mathbb{R}^n$ are the reaction terms, linking the macroscopic action potential propagation to the cellular dynamics. The unknown \mathbf{w} is a n -th dimensional vector function fulfilling a system of differential algebraic equations representing the percentage of open channels per unit area of the membrane. Specifically, we used the Courtemanche-Ramirez-Nattel (CRN, $n = 20$) in case of atrial action potential and the Ten-Tusscher-Panfilov (TTP, $n = 18$) for the ventricular one (for further details see [77] for CRN and [78] for TTP). Furthermore, system (6) is equipped with suitable initial conditions for u and \mathbf{w} and homogeneous Neumann boundary conditions for u at the boundary $\partial\Omega$.

4.2 Numerical approximation

For the time discretization of the monodomain system (6) we introduce the discrete times $t^n = n\Delta t$, $n \geq 0$, and, given a function of time $z(t)$, we denote by z^{n+1} the approximation of $z(t^{n+1})$. Then, at each time step t^{n+1} we consider a *Backward Difference Formulae* approximation of order $\sigma = 1, 2, 3$ (BDF $_\sigma$) with an explicit treatment of the reaction term, obtaining the following semi-discretized in time formulation:

$$\frac{\alpha_{\text{BDF}\sigma} \mathbf{w}^{n+1} - \mathbf{w}_{\text{BDF}\sigma}^n}{\Delta t} + \mathbf{G}(u_{\text{EXT}\sigma}^{n+1}, \mathbf{w}_{\text{EXT}\sigma}^{n+1}) = 0, \quad \text{in } \Omega, \quad (7a)$$

$$\chi C_m \frac{\alpha_{\text{BDF}\sigma} u^{n+1} - u_{\text{BDF}\sigma}^n}{\Delta t} - \nabla \cdot (\mathbb{D} \nabla u^{n+1}) + \chi I_{ion}(u_{\text{EXT}\sigma}^{n+1}, \mathbf{w}^{n+1}) = I_{app}^{n+1}, \quad \text{in } \Omega, \quad (7b)$$

where $u_{\text{BDF}\sigma}^n = \sum_{i=0}^{\sigma-1} \alpha_i u^{n-i}$, $\mathbf{w}_{\text{BDF}\sigma}^n = \sum_{i=0}^{\sigma-1} \alpha_i \mathbf{w}^{n-i}$, $u_{\text{EXT}\sigma}^{n+1} = \sum_{i=0}^{\sigma-1} \beta_i u^{n-i}$ and $\mathbf{w}_{\text{EXT}\sigma}^{n+1} = \sum_{i=0}^{\sigma-1} \beta_i \mathbf{w}^{n-i}$ are extrapolations of order σ of solutions computed at the previous time steps, with $\alpha_{\text{BDF}\sigma}$, α_i , β_i suitable coefficients depending on the order σ (refer to Table 4 for their specific values). Moreover, the diffusion term is treated implicitly, whereas the ionic terms explicitly. At each time step we first update the gating variables \mathbf{w}^{n+1} given $\mathbf{w}_{\text{BDF}\sigma}^n$, $u_{\text{EXT}\sigma}^{n+1}$ and $\mathbf{w}_{\text{EXT}\sigma}^{n+1}$ by

BDF σ	$\alpha_{\text{BDF}\sigma}$	α_0	α_1	α_2	β_0	β_1	β_2
BDF1	1	1	-	-	1	-	-
BDF2	3/2	2	-1/2	-	2	-1	-
BDF3	11/6	3	-3/2	1/3	3	-3	1

Table 4: Characteristic values of the considered BDF σ time discretization (with $\sigma = 1, 2, 3$) of the monodomain system (7).

means of (7a), then we solve (7b) for u^{n+1} using $u_{\text{EXT}\sigma}^{n+1}$ and the up-to-date gating variables \mathbf{w}^{n+1} . This type of time discretization leads to a conditionally stable method with a time step Δt bound (independent of the space discretization) which is milder than that required to capture the propagating wave front [75, 80, 83].

Regarding the space discretization, we used continuous Finite Elements (FE) on hexahedral meshes. The discretization of the ionic current term I_{ion} is performed following the Ionic Current Interpolation (ICI) approach [84]: first, $I_{ion}(u, \mathbf{w})$ is evaluated at each nodal points and then it is interpolated at quadrature nodes. The ICI method is less memory-demanding than computing I_{ion} directly at quadrature nodes and it is not affected by numerical accuracy issues at small mesh size required to capture the propagating front [46]. Finally, we solved the linear system coming from the space discretization of (7b) with the GMRES method [85] preconditioned with the Jacobi preconditioner.

5 Numerical results

This section is dedicated to several results both for the fibers generation and the numerical electrophysiology simulations. These have been performed both on idealized and realistic human ventricular and atrial models. As realistic geometry, we use the Zygote solid 3D heart model [86], a complete heart geometry reconstructed from high-resolution CT-scans representing an average healthy heart. Being a very detailed model of the human heart, it demonstrates the applicability of the proposed methods to arbitrary patient-specific scenarios.

We organize the section as follows. After a brief description related to the setting of numerical simulations (Section 5.1), we address the issue of estimating the parameters used in the electrophysiology simulations (Section 5.2). In Section 5.3, we show various comparisons among the three LDRBMs for ventricles fiber generation presented in Section 2: we compare the fiber orientations and we analyse their influence in terms of activation times computed as output of numerical electrophysiology simulations³. For this comparison, first we make use of an idealized biventricular geometry built using the prolate spheroid coordinate

³The activation time of a given point in the cardiac muscle is defined as the time when the transmembrane potential derivative $\frac{du}{dt}$ reaches its maximal value.

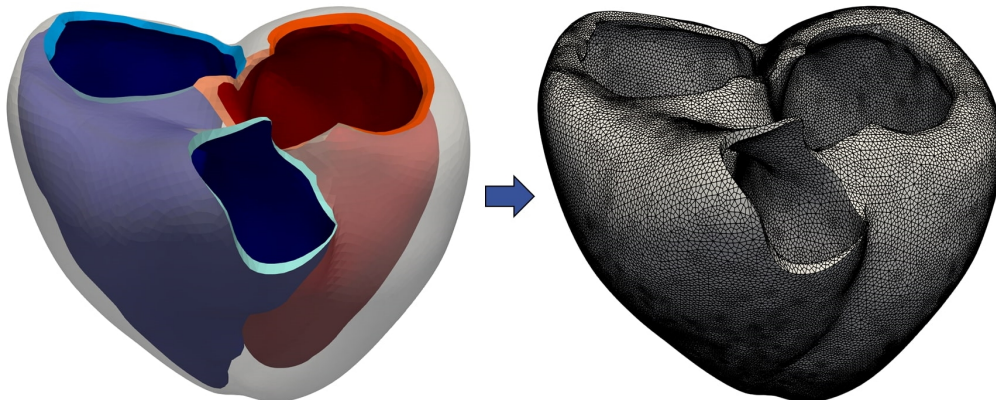


Figure 6: Processing pipeline applied to build a ventricles FE mesh [90]. Left: smoothing and tagging procedure; Right: FE mesh of hexahedral elements.

systems [87], and then we consider the Zygote biventricular model [86]. Section 5.4 is devoted to the novel atrial LDRBM. We show fiber bundles reconstruction applied to idealized [88] and the realistic Zygote [86] geometries. Afterwards, we investigate the influence of atrial fibers in electrophysiology simulations comparing the fiber activation map with respect to a one obtained with an isotropic conductivity. Finally, in Section 5.5 we present an electrophysiology simulation of a realistic four chamber heart including fibers generated by LDRBMs for both atria and ventricles.

5.1 Setting of numerical simulations

To build FE meshes, a pre-processing pipeline was applied to every ventricular and atrial geometry used in the simulations. This pipeline consists of multiple steps including tagging, geometry smoothing and hexahedral FE mesh generation. Specifically, the Vascular Modelling Toolkit `vtk` software [89] (<http://www.vmtk.org>) together with a new meshing tool [90] were used to perform this pre-processing phase. In Figure 6 we report the former pipeline applied to build a realistic biventricular FE mesh (for further details about the pre-processing pipeline refer to [90]).

All the LDRBMs for the ventricles (presented in Section 2), the novel atrial LDRBM (detailed in Section 3) and the numerical methods for the electrophysiology presented in Section 4.2 have been implemented within `lifex` (<https://lifex.gitlab.io/lifex>), a new in-house high-performance C++ FE library mainly focused on cardiac applications based on `deal.II` FE core [91] (<https://www.dealii.org>). All the numerical simulations were executed on the cluster `iHeart` (Lenovo SR950 8x24-Core Intel Xeon Platinum 8160, 2100 MHz and 1.7TB RAM) at MOX, Dipartimento di Matematica, Politecnico di Milano.

To analyse the results we used `ParaView` (<https://www.paraview.org>) an

Muscle type (ionic model)	σ_f [mS/cm]	σ_s [mS/cm]	σ_n [mS/cm]
Ventricles (TTP)	1.07	0.49	0.16
Atria (CRN)	7.00	0.77	0.77

Table 5: Conductivity values σ_f , σ_s and σ_n obtained after the fitting procedure, displayed in Figure 7, for the ventricles (using TTP) and for the atria (using CRN).

open-source, multi-platform data analysis and visualization application. In particular, to visualize the fiber fields we applied in sequence the `streamtracer` and the `tube ParaView` filters.

5.2 On the choice of physical and numerical parameters

We report the choices of parameters involved in the numerical approximation of the monodomain system (6). The latter requires the following physical data: the transmembrane capacitance per unit area C_m , the membrane surface-to-volume ratio χ and the conductivities along the three direction of the myofibers σ_f , σ_s and σ_n appearing in the conductivity tensor \mathbb{D} . The values chosen for the first two quantities are $C_m = 1 \mu\text{F}/\text{cm}^2$ and $\chi = 1400 \text{ cm}^{-1}$, which are within the physiological acceptable range of values reported in [24, 76, 92, 93].

The conductivity values σ_f , σ_s and σ_n were fitted by an iterative procedure described in [94] (see also [23, 45]) in order to match the following conduction velocity values: for the ventricles, 60 cm/s in the fiber direction \mathbf{f} , 40 cm/s in the sheet direction \mathbf{s} and 20 cm/s in the normal direction \mathbf{n} [45]; for the atria, 120 cm/s in the fiber direction \mathbf{f} and 40 cm/s along the sheet \mathbf{s} and cross-fiber directions \mathbf{n} [23]. In Figures 7(a) and 7(b) we show the results of this fitting procedure. The estimated values for σ_f , σ_s and σ_n , reported in Table 5, lay within the confidence interval for the experimentally measured conductivity values reported in [2, 95, 96, 97, 98, 99].

Finally, to initiate the signal propagation in the cardiac muscle, the monodomain system (6) requires to specify the external applied current $I_{app}(\mathbf{x}, t)$. In this work $I_{app}(\mathbf{x}, t)$ represents a series of impulses (with radius 2.5 mm and duration 3 ms) applied in spherical subsets of the domain and prescribed alongside the ventricles and atria endocardium. Its amplitude is $50000 \mu\text{A}/\text{cm}^3$, for both atria and ventricle domains, in agreement with [93]: this represents the lowest value allowing the electrical signal to develop. We used this value for all the simulations performed in this work, while the stimuli locations will be specified for each case reported in Sections 5.3, 5.4 and 5.5.

Regarding the mesh element size h and the time step Δt , related to the space and time discretizations of the system (6), accuracy constraints are imposed when biophysical models (as CRN [77] and TTP [78]) are used: $h = 100\text{--}500 \mu\text{m}$ and $\Delta t = 1\text{--}50 \mu\text{s}$ [80, 83, 93]. These strong restrictions are motivated

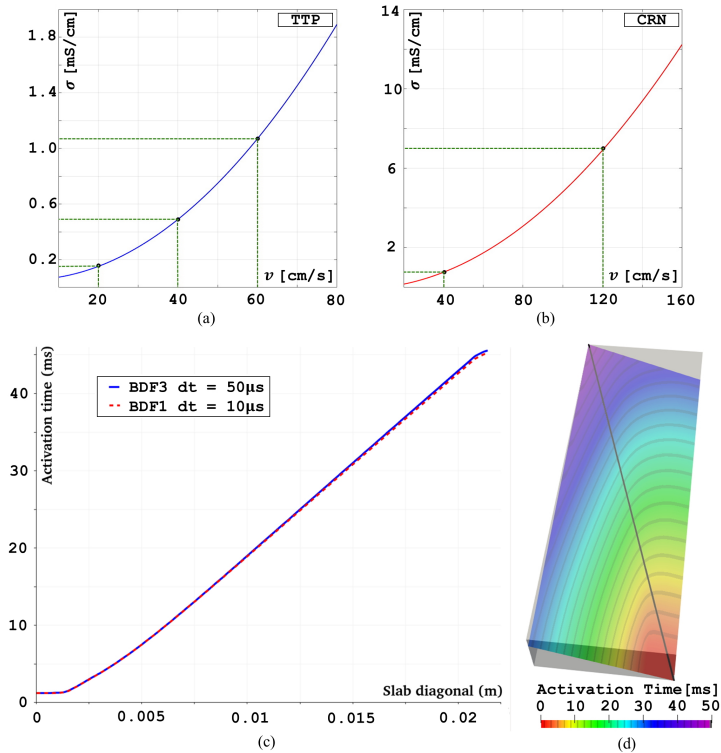


Figure 7: Top (a,b): Fitting procedure used to estimate the conductivity σ required to match specific conduction velocity v [94]; (a): using the TTP ionic model to obtain 60, 40 and 20 cm/s; (b): using the CRN ionic model to obtain 120 and 40 cm/s. The values for σ_f , σ_s and σ_n are reported in Table 5. Bottom (c,d): Comparison between BDF3 and BDF1 time discretization for the monodomain system (6) in the slab benchmark problem [93]; (c): plot of the activation time alongside the slab diagonal (displayed in black on the Right); Red: BDF1; Blue: BDF3. (d): activation time in a clipped slice of the slab for BDF3 time discretization.

mainly by the fast upstroke of cellular depolarization which produces a step-like wavefront over a small spatial extent [100]. For the space discretization, we used continuous FE of order 1 (Q_1) on hexahedral meshes with an average mesh size of $h = 350 \mu\text{m}$, an acceptable value at least for linear finite element approximation and for physiological cases [42, 46, 101, 102, 103]. Concerning the time discretization, we used the BDF of order $\sigma = 3$ with a time step of $\Delta t = 50 \mu\text{s}$. Although, the most common time discretization used in literature for the monodomain system (6) is the BDF1 (commonly known as the backward Euler method), which requires a time step at most of $10 \mu\text{s}$ [83], BDF3 allows us to use a larger value of Δt to obtain the same accuracy of BDF1. To confirm this, in Figures 7(c) and 7(d) we report a comparison between BDF3 with $\Delta t = 50 \mu\text{s}$ and BDF1 $\Delta t = 10 \mu\text{s}$ on a benchmark problem proposed in [93]. BDF3

requires more storage than BDF1, however this extra cost is largely repaid by the computational time saved in our simulations using a larger time step.

5.3 Ventricular fibers generation and electrophysiology

This section is dedicated to the comparison among the different fiber fields generated by the three ventricular LDRBMs presented in Section 2. Moreover, we also investigate the influence of the different fibers orientation in the activation times, produced by electrophysiology simulations. We perform both the analyses first in an idealized biventricular geometry [104] and then in the Zygote realistic human model [86].

5.3.1 Idealized biventricular model

The first comparison among the three ventricles LDRBMs was performed on a well established idealized biventricular geometry that has been used in several computational studies [18, 87, 104, 105, 106, 107] and for ventricles volume estimation from 2D images [108]. The heart ventricles are approximated as two intersecting truncated ellipsoids.

We constructed the idealized biventricular geometry using the prolate spheroid coordinate systems in the built-in CAD engine of `gmsh`, an open source 3D finite element mesh generator (<http://gmsh.info>), see Figure 8. For the details about the geometrical definition of the idealized biventricular, we refer to [104, 107].

5.3.1.1 Idealized ventricles fiber generation

Fiber orientations obtained for the three LDRBMs (R-RBM, B-RBM and D-RBM) in the idealized biventricular model are shown in Figures 8(a-f). The input angles values $\alpha_{endo,\ell}$, $\alpha_{epi,\ell}$, $\alpha_{endo,r}$, $\alpha_{epi,r}$, $\beta_{endo,\ell}$, $\beta_{epi,\ell}$, $\beta_{endo,r}$ and $\beta_{epi,r}$ were chosen for all the three methods based on the observations of histological studies in the human heart [12, 29, 31, 53, 54, 109, 110] (see also [20]):

$$\begin{aligned} \alpha_{epi,\ell} &= -60^\circ, & \alpha_{endo,\ell} &= +60^\circ, & \alpha_{epi,r} &= -25^\circ, & \alpha_{endo,r} &= +90^\circ; \\ \beta_{epi,\ell} &= +20^\circ, & \beta_{endo,\ell} &= -20^\circ, & \beta_{epi,r} &= +20^\circ, & \beta_{endo,r} &= 0^\circ. \end{aligned} \quad (8)$$

We observe that all the LDRBMs represent the characteristic helical structure of the left ventricle and a compatible fiber orientations both in the right endocardium, not facing to the septum, and in the right epicardium, far enough from the inter-ventricular junctions. Most of the differences occur in the right ventricle endocardium facing the septum (see Figures 8(a-c)) and in the inter-ventricular junctions between the two ventricles (see Figures 8(d-f)). Indeed, as expected by construction of the methods, for R-RBM the fibers in the whole septum belong to the left ventricle, while in B-RBM and D-RBM they are shared between the two ventricles. In particular, for B-RBM the septum is equally split between the two ventricles, while D-RBM associates two-third of septum to

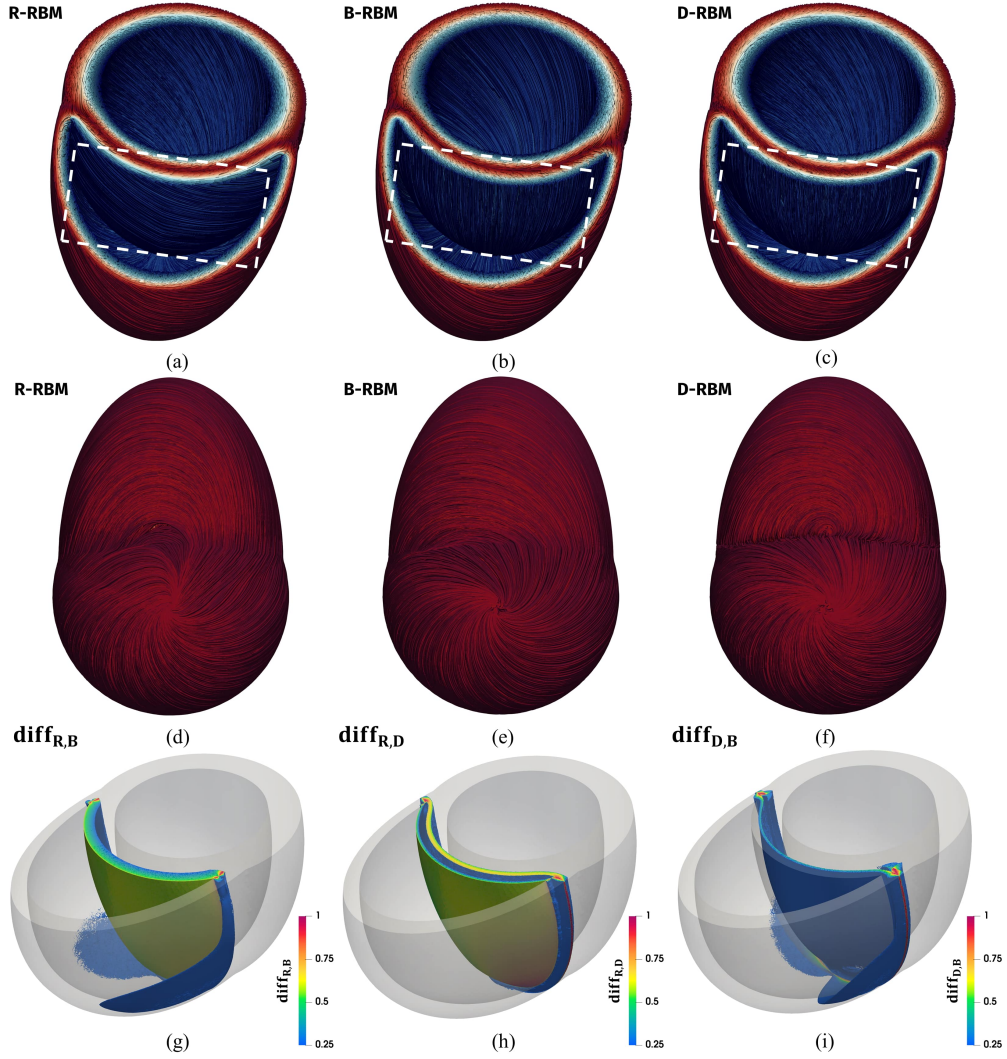


Figure 8: Comparison among LDRBMs in the idealized biventricular model. Streamlines of the vector \mathbf{f} is depicted for R-RBM (a,d), B-RBM (b,e) and D-RBM (c,f). Top: Frontal view (dashed box highlights the differences among the three LDRBMs in the septal region); Centre: apex view; Bottom: Differences $\text{diff}_{i,j}$ among the three LDRBMs, $\text{diff}_{R,B}$ (g), $\text{diff}_{R,D}$ (h) and $\text{diff}_{D,B}$ (i); only values $\text{diff}_{i,j} \geq 0.25$ are displayed.

the left ventricle and one third to the right one. As a consequence, only for B-RBM and D-RBM the fibers direction is preserved in all the right endocardium, see Figures 8(a), 8(b) and 8(c). In the inter-ventricular junctions, both R-RBM and B-RBM exhibit a smooth transition passing from left to right ventricle (see Figures 8(c) and 8(d)), while in D-RBM there is an abrupt change in the fiber directions (see Figure 8(e)). Moreover, in D-RBM it is possible to see the fibers

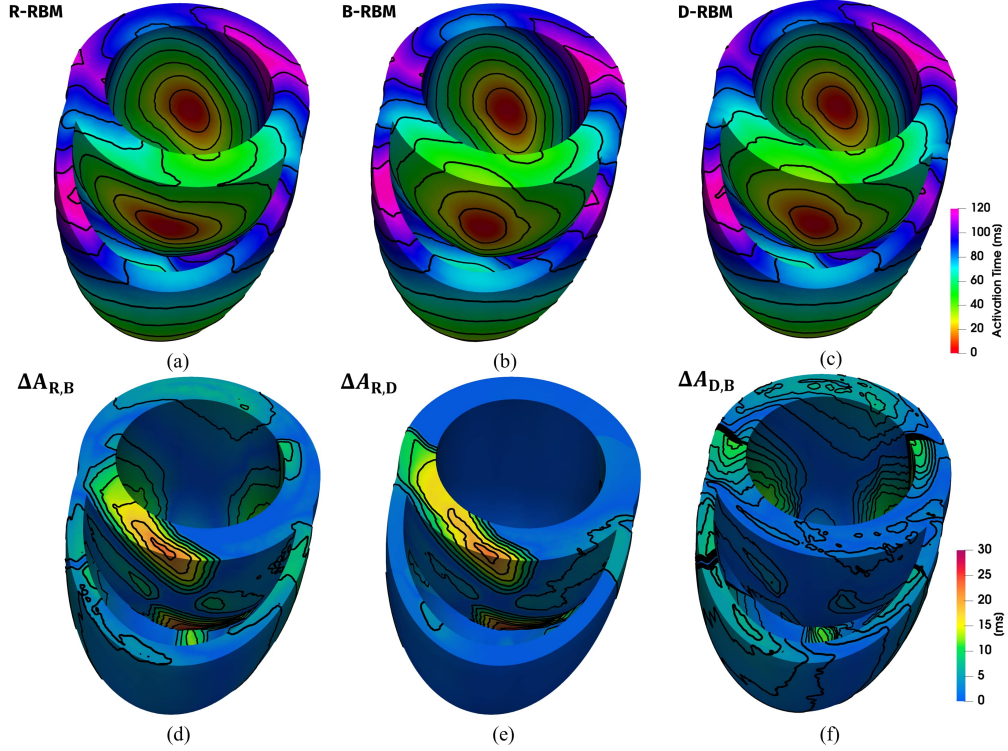


Figure 9: Top: Activation time for R-RBM (a), B-RBM (b) and D-RBM (c) in the idealized biventricular model. Bottom: Absolute difference among the activation maps, $\Delta A_{R,B}$ (d), $\Delta A_{R,D}$ (e) and $\Delta A_{D,B}$ (f).

winding around the right ventricle apex (see Figure 8(e)). This feature is not present in the R-RBM and B-RBM, see Figures 8(c) and 8(d). All the aforementioned discrepancies are caused by the different transmural and normal direction definitions of the three LDRBMs (explained in detail in Section 2).

We computed the difference $\text{diff}_{i,j}$ of the fiber field \mathbf{f} among the three methods, defined as:

$$\text{diff}_{i,j}(\mathbf{x}) = 1 - |\mathbf{f}_i(\mathbf{x}) \cdot \mathbf{f}_j(\mathbf{x})| \quad i, j = R, B, D \quad (i \neq j), \quad (9)$$

where \mathbf{f}_R , \mathbf{f}_B and \mathbf{f}_D are the vector fiber fields of R-RBM, B-RBM and D-RBM, respectively. If \mathbf{f}_i and \mathbf{f}_j are parallel, $\text{diff}_{i,j} = 0$, otherwise, when orthogonal, $\text{diff}_{i,j} = 1$. The result of these comparisons is reported in Figures 8(g), 8(h) and 8(i). As expected, most of the discrepancies are in the septum and in the inter-ventricular junctions.

5.3.1.2 Idealized ventricles electrophysiology

In order to evaluate the influence of the three LDRBMs fiber architectures in the electric signal propagation through the cardiac muscle, we performed three

electrophysiology simulations (with the setting detailed in Section 5.2), one for each LDRBM. To initiate the action potential propagation we applied four endocardial stimuli: two for each ventricle, one in the mid-septal zone and one in the posterior endocardium. In Figures 9(a-c) we report the activation maps obtained with the three fibers configurations. The activation pattern for all the three methods are very similar in the left and right ventricles, while most of the differences are visible in the septum, see Figures 9(a), 9(b) and 9(c). We computed also the absolute difference $\Delta A_{i,j}(\mathbf{x})$ in the activation pattern among the different methods as:

$$\Delta A_{i,j}(\mathbf{x}) = |A_i(\mathbf{x}) - A_j(\mathbf{x})| \quad i, j = R, B, D \quad (i \neq j), \quad (10)$$

where A_R , A_B and A_D are the activation times for R-RBM, B-RBM and D-RBM, respectively (see Figures 9(d), 9(e) and 9(f)).

The most remarkable differences in both $\Delta A_{R,B}$ and $\Delta A_{R,D}$ are exhibited in the septum, particularly in the part facing the right endocardium, while $\Delta A_{B,D}$ never exceeds 15 ms, see Figures 9(d), 9(e) and 9(f). Also in the activation maps, as expected, we retrieve differences in the septum zone caused by the different fibers definition on that region made by the three methods, as seen in the fibers comparison, see Figures 8.

Finally, we evaluated the maximal discrepancies, $M_{i,j} = \max_{\mathbf{x} \in \Omega_{myo}} \Delta A_{i,j}(\mathbf{x})$, among the three methods, which are:

$$M_{R,B} = 35 \text{ ms}, \quad M_{R,D} = 33 \text{ ms}, \quad M_{B,D} = 15 \text{ ms}.$$

The location of both $M_{R,B}$ and $M_{R,D}$ is in the lower part of the right ventricle septum, while $M_{B,D}$ is placed in the lower anterior region of the left ventricle, see Figures 9(d), 9(e) and 9(f). Considering a total activation time of about $A_{max} = 120$ ms for the all biventricular muscle, the maximum relative differences, $M_{i,j}^{\%} = M_{i,j}/A_{max}$, among the three ventricle LDRBMs are

$$M_{R,B}^{\%} = 29\%, \quad M_{R,D}^{\%} = 28\%, \quad M_{B,D}^{\%} = 13\%.$$

5.3.2 Realistic full biventricular model

The second comparison among the ventricular LDRBMs was performed on a realistic full biventricular geometry. For this purpose, we used the Zygote solid 3D heart model [86]. In order to obtain a smooth endocardium in both ventricles, we removed all the papillary muscles and the trabeculae carneae, using the CAD modeller SolidWorks (<https://www.solidworks.com>) in combination with the software Meshmixer (<http://www.meshmixer.com>), see Figure 10. Considering the characteristics of the electrical signal propagation, and the anatomical constituents of the valvular and sub-valvular apparatus, we expect our calculations should not be substantially influenced by the papillary muscles elimination.

According to the motivations highlighted at the end of Section 2, we performed a comparison in the full biventricular model only between B-RBM and D-RBM.

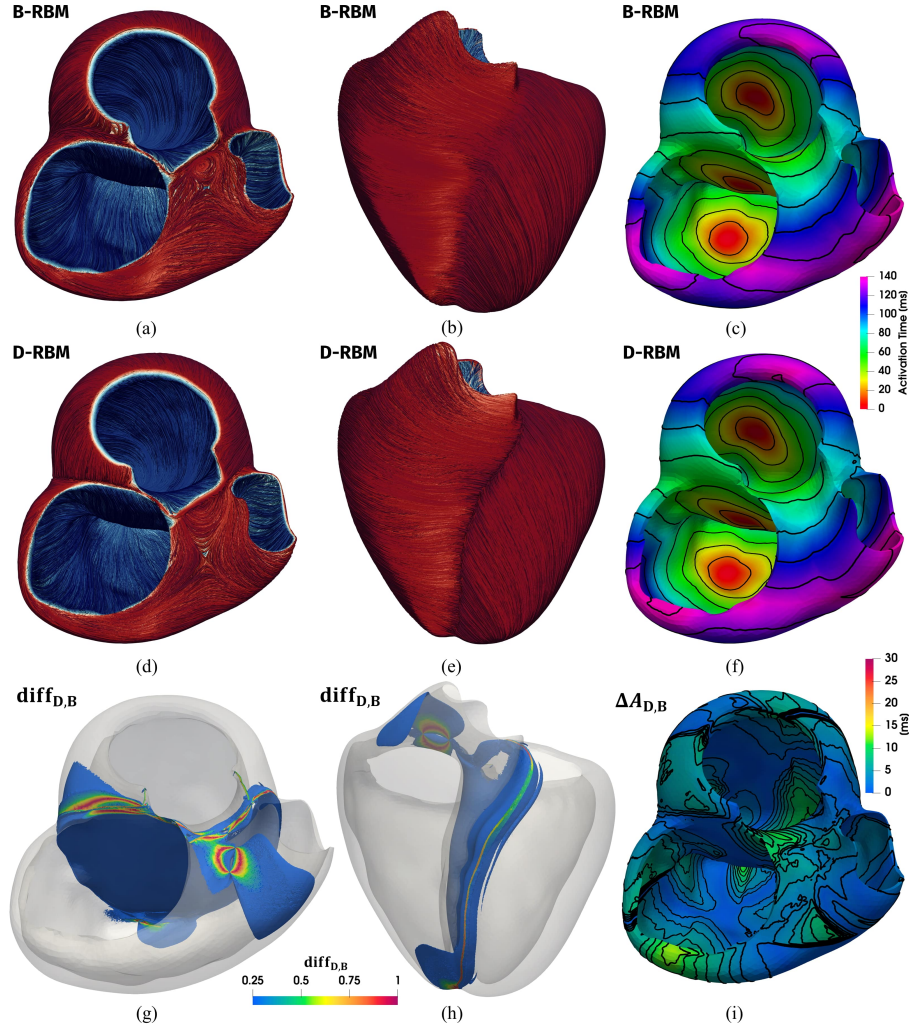


Figure 10: Comparison for B-RBM and D-RBM in a realistic full biventricular model. Top (a-c): B-RBM. Centre (d-f): D-RBM. Bottom (g-i): differences between B-RBM and D-RBM. Streamlines of the vector \mathbf{f} : top (a,d) and lateral views (b,e). Difference in the fiber orientations $\text{diff}_{D,B}$ (g,h), only the values $\text{diff}_{i,j} \geq 0.25$ are displayed. Activation maps using B-RBM and D-RBM: B-RBM (c) and D-RBM (f). Absolute difference among B-RBM and D-RBM activation maps, $\Delta A_{D,B}$ (i).

5.3.2.1 Realistic ventricles fibers generation

Fiber orientation for B-RBM and D-RBM in the Zygote full biventricle are displayed in Figures 10(a-b) and 10(d-e). We prescribed the same input angle values used for the ideal geometry, reported in (8). Moreover, for D-RBM we

have also specified the angles in the OT regions as follows [20]:

$$\alpha_{epi,OT} = 0^\circ, \quad \alpha_{endo,OT} = +90^\circ, \quad \beta_{epi,OT} = 0^\circ, \quad \beta_{endo,OT} = 0^\circ. \quad (11)$$

The two LDRBMs well reproduce the helical structure of the left ventricle up to the mitral valve ring and exhibit a similar fiber orientation pattern in whole cardiac muscle, apart from the region between the tricuspid, the pulmonary and the aortic valve rings and far enough from the inter-ventricular junctions, see Figures 10(a-b) and 10(d-e). B-RBM presents a roll up in the fiber directions just after the aortic valve ring, while D-RBM has a more longitudinal fiber orientations in that region, see Figure 10(a) and 10(d). As also observed in the idealized case, the B-RBM fiber field in the inter-ventricular junctions has a smooth change passing from the left to the right ventricle, whereas D-RBM produces a strong discontinuity in the transition across the two ventricles, see Figure 10(b) and 10(e).

We evaluated the mismatch of the fiber fields $\text{diff}_{D,B}$, defined in (9), between B-RBM and D-RBM. Also in this case, the discrepancies are caused by the different transmural and normal direction definitions of the two methods (as detailed in Section 2). Indeed, $\text{diff}_{D,B}$ highlights the most relevant differences of the two methods in the septum, in the inter-ventricular junctions, in the regions of tricuspid, pulmonary and aortic valve rings and around the right ventricle apex, see Figures 10(g) and 10(h).

5.3.2.2 Realistic ventricles electrophysiology

We performed two electrophysiology simulations (with the setting detailed in Section 5.2), one with B-RBM and one with D-RBM. Two stimuli were applied to each ventricle: one in the mid-septal zone and one in the posterior endocardium. Figures 10(c) and 10(f) depict the computed activation times which result very similar in the whole myocardium. Figure 10(i) shows the absolute difference between the two activation maps, $\Delta A_{D,B}(\mathbf{x}) = |A_D(\mathbf{x}) - A_B(\mathbf{x})|$, where A_B and A_D are the activation times for B-RBM and D-RBM, respectively. We observe some discrepancies in the activation pattern near the tricuspid, the aortic and the pulmonary valve rings, and also in the endocardium near the right ventricle apex, although $\Delta A_{D,B}$ never exceeds the value 14 ms, see Figure 10(i). The maximal relative discrepancy among the two methods is $M_{D,B} = \max_{\mathbf{x} \in \Omega_{myo}} \Delta A_{D,B}(\mathbf{x}) = 14$ ms, corresponding to $M_{D,B}^{\%} = M_{D,B}/A_{max} = 10\%$, with $A_{max} = 140$ ms the total activation time. The location of $M_{D,B}$ is in the lower part of the endocardium just above the right ventricle apex, see Figure 10(i).

5.4 Atrial fibers generation and electrophysiology

We applied our new atrial LDRBM (presented in Section 3) to reconstruct left and right atria fiber architecture, first in idealized geometries [88] and then in realistic ones [86]. We analysed the influence of atrial fiber bundles in the

electric signal propagation by means of electrophysiology simulations performed on realistic geometries. Finally, we studied how a change in size of a single bundle affects the total activation sequence.

5.4.1 Atrial fibers generation

We began applying the novel atrial LDRBM on idealized geometries. To construct them, we started by the surface representations of the right and left atrium generated as separated NURBS patches, as reported in [88, 111]. For each atrium, we created the corresponding triangular mesh using the constructive geometry module of `Netgen` (<https://ngsolve.org>). We considered this triangular mesh as the endocardium of our 3D model. To generate the atria epicardium we extruded (using the `vtk` software [89]) the endocardial surface by 2 mm, which correspond to an average thickness of the atrial wall [16, 112]. Finally, we produced 3D tagged hexahedral mesh following the preprocessing pipeline described in Section 5.1, and then we applied our atrial LDRBM, see Figures 11(a-d).

Afterwards, we treated the case of realistic left and right atria taken from the Zygote 3D heart model [86]. Figures 11(e-h) show the corresponding fibers generated by our atrial LDRBM.

LA	τ_{avr}	τ_{lpv}	τ_{rpv}	RA	τ_{avr}	τ_{icv}	τ_{scv}	τ_{ct+}	τ_{ct-}	τ_{fw}	τ_{sw}	τ_r
Ideal	0.65	0.65	0.10	Ideal	0.90	0.90	0.10	-0.10	-0.18	0.01	0.135	0.55
Real	0.85	0.85	0.20	Real	0.90	0.85	0.30	-0.55	-0.60	-0.25	-0.10	0.60

Table 6: Bundles parameters used for fibers generation in the idealized (Ideal) and realistic (Real) LA and RA.

The input values of the parameters τ_i , which define the bundles dimension of the atrial LDRBM, are reported in Table 6. We observe that the atrial LDRBM qualitatively capture the complex arrangement of fiber directions in almost all the principal anatomical atrial regions (see Figure 11): in the right atrium (RA), superior (SCV) and inferior caval veins (ICV), tricuspid valve ring (TV), right appendage (RAA), septum (RAS), inter-caval bundle (IB), crista terminalis (CT), isthmus (IST) and later wall (RAW); for the left atrium (LA), left (LPV) and right pulmonary veins (RPV), mitral valve ring (MV), left appendage (LAA), septum (LAS), septum wall (LSW), lateral wall (LAW) and roof (LAR).

Circular fiber arrangements are exhibited around LPV, RPV, SCV, ICV, TV, MV, and encircle both appendages (RAA and LAA), see Figures 11(a-d) and 11(e-g). Fibers direction of CT runs longitudinally from the base of the SCV to the ICV, see Figures 11(d) and 11(h). RA structures like the IB and RAW are almost vertically oriented, whereas those of RAS are parallel to the CT, see Figures 11(c-d) and 11(g-h). IST fibers have the same direction of those

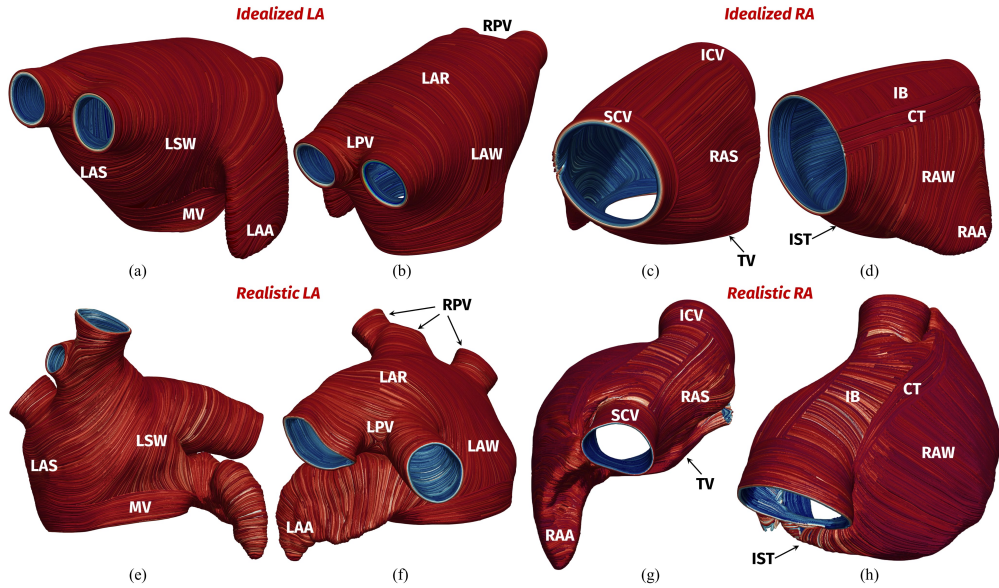


Figure 11: Atrial LDRBM fiber generation applied to idealized (a-d) and realistic (e-h) atria models. Frontal (a,c,e,g) and dorsal (b,d,f,h) views of the atria. SCV, ICV: superior and inferior caval veins; LPV, RPV: left and right pulmonary veins; TV, MV: tricuspid and mitral valve rings; RAA, LAA: right and left appendage; RAS, LAS: right and left septum; RAW, LAW: right and left later wall; LSW: left septum wall; LAR: left atrial roof; IB: inter-caval bundle; CT: crista terminalis; IST: isthmus.

of the TV, see Figures 11(d) and 11(h). The LAS fibers are aligned with the adjacent region of RAS, see Figures 11(a) and 11(e). Directions of the LAR and LAW descend perpendicularly to MV (Figures 11(b) and 11(f)), while fibers of LSW present a smooth transition going to the LAS and LAA (Figures 11(a) and 11(e)). We observed that these behaviours of atrial fibers direction showed a good agreement with histological studies [64, 65, 8, 113] and other published RBMs [16, 21, 27, 23, 35, 114].

5.4.2 Atrial electrophysiology

In order to analyse the influence of atrial fiber bundles in the electric signal propagation we performed several electrophysiological simulations (with the setting specified in Section 5.1) on the realistic Zygote atrial geometries.

Firstly, we made a comparison with an isotropic model. For the atrial LDRBM, we considered the parameters detailed in Table 6, while the isotropic simulations were carried out by setting in (5) $\sigma_f = \sigma_s = \sigma_n = 7.0$ mS/cm, that is a representative value chosen for the conductivity along the atrial fiber direction, see Table 5. To initiate the signal propagation in the RA we applied a single

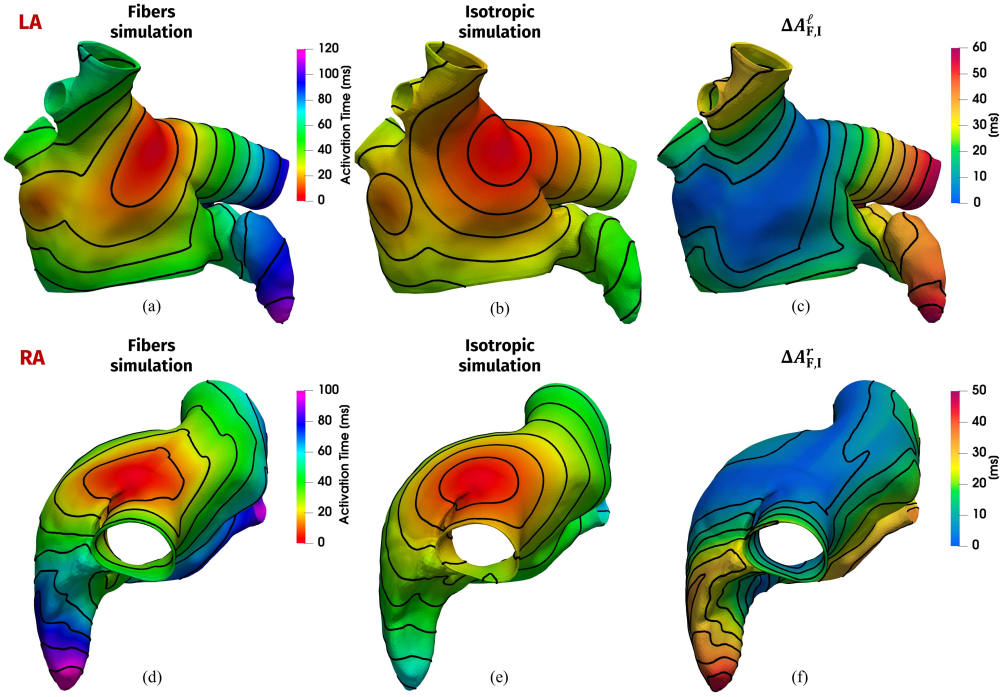


Figure 12: Comparison between the activation maps of electrophysiology simulations performed with the atrial LDRBM fiber generation and the isotropic model. Left (a,d): Fibers simulation; Centre (b,e): Isotropic simulation. Right (c,f): absolute difference $\Delta A_{F,I}^i$ in the activation times for LA ($i = \ell$) and RA ($i = r$). Top (a,b,c): LA; Bottom (d,e,f): RA.

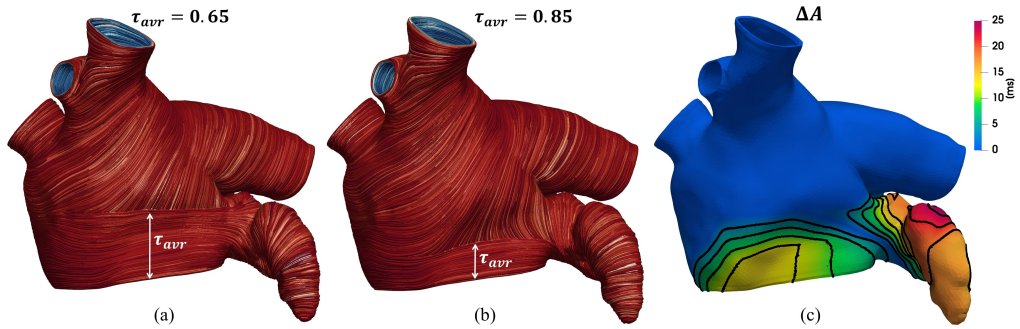


Figure 13: Comparison between electrophysiology simulations with different values of τ_{avr} in the atrial LDRBM fiber generation for the Zygote LA. Left (a): $\tau_{avr} = 0.65$; Centre (b): $\tau_{avr} = 0.85$; Right (c): absolute difference ΔA .

stimulus in the Sino-Atrial-Node (SAN) which lies in the musculature of CT at the anterolateral junction with the SCV [65]. For the LA we stimulated the main inter-atrial connections: the Bachman's Bundle (BB), located in the LSW; the

upper part of the Fossa Ovalis (FO) in the centre of LAS; the Coronary Sinus Musculature limbs (CSM) placed at the bottom of LAW [115]. Activation of FO and CSM was delayed, with respect to the BB stimulus, by 14 ms and 52 ms, respectively.

Figure 12 displays the results of the comparison among simulations performed with the atrial LDRBM fibers and the isotropic model for both the RA and LA. Both the activation pattern and activation time present significant differences. To provide a quantification, we computed the absolute difference $\Delta A_{F,I}^i$ in the activation time:

$$\Delta A_{F,I}^i(\mathbf{x}) = |A_{F,I}^i(\mathbf{x}) - A_I^i(\mathbf{x})| \quad i = r, \ell, \quad (12)$$

where $i = r, \ell$ refer to LA ($i = \ell$) and RA ($i = r$) and $A_{F,I}^i$ and A_I^i are the activation times obtained by the simulations with and without fibers, respectively. Most of the differences occur at LPV and LAA for LA, and at RAA and TV for RA. Finally, we computed the maximal discrepancy, $M_{F,I}^i = \max_{\mathbf{x} \in \Omega_{atrial}} \Delta A_{F,I}^i(\mathbf{x})$, $i = \ell, r$:

$$M_{F,I}^{\ell} = 60 \text{ ms (52 \%)}, \quad M_{F,I}^r = 48 \text{ ms (44 \%)},$$

where in brackets we reported the relative values computed as $M_{F,I}^i/A_{max}^i$, with $A_{max}^{\ell} = 116$ ms and $A_{max}^r = 108$ ms the total activation times. For RA $M_{F,I}^r$ is placed in RAA, while for LA $M_{F,I}^{\ell}$ is located in LPV.

Then, we investigated how a local change in a single LA bundle (the atrioventricular one) affects the total activation pattern. We performed two electrophysiology simulations with the same fiber setting used for the comparison with an isotropic model, except for the value of τ_{avr} , which was set equal to 0.65 and 0.85. Figures 13(a-b) depict the corresponding generated fibers: notice that with $\tau_{avr} = 0.65$ the avr-bundle is thicker with respect to the one obtained with $\tau_{avr} = 0.85$, see Figures 13(a-b). We also reported the absolute difference in the computed activation times for the two fiber architectures, see Figure 13(c). The maximal discrepancy, located in the LAA, is of 28 ms which corresponds to 24% of the total activation time for the LA (116 ms).

5.5 Whole heart fibers and electrophysiology

In this section we present the whole heart fiber generation, using LDRBMs for both atria and ventricles. Moreover, we show an electrophysiology simulation using physiological activation sites and including the fiber generated by LDRBMs. We use the Zygote heart model [86] both for the full biventricle and the atria geometries introduced in Sections 5.3.2 and 5.4, respectively.

5.5.1 Whole heart fibers

For the fibers generation, we adopted D-RBM [20] (see Section 2) for the ventricles, with the same setting of Section 5.3.2, and the proposed LDRBM for the

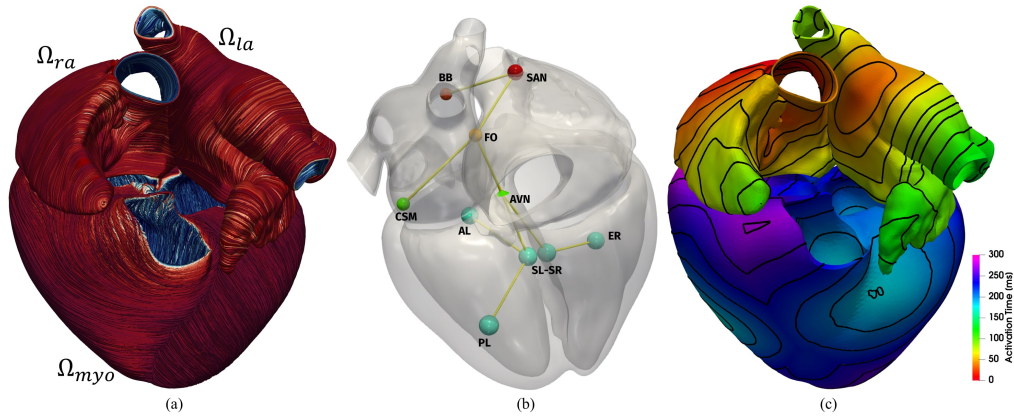


Figure 14: Left (a): Fiber generation applied to realistic Zygote Heart model; LDRBM by Doste (D-RBM) was applied to reconstruct the ventricles fibers on Ω_{myo} , while the atrial LDRBM was employed for the atria fiber architecture on Ω_{ra} and Ω_{la} . Centre (b): Stimuli applied in the four chamber model to mimic the Cardiac Conduction System (CCS) pathway; SAN: Sino-Atrial Node; BB: Bachmann’s Bundle; FO: Fossa Ovalis; CSM: Coronary Sinus Musculature; AVN: Atrio-Ventricular Node; AL: Left Anterior; PL: Left Posterior; SL, SR: Left and Right Septum; ER: Right Endocardium. Right (c): activation maps computed from the electrophysiology simulation.

atria (see Section 3), with the configuration of Section 5.4 (see also Table 6). Figure 14(a) displays the heart geometry equipped with the prescribed LDRBMs fibers.

5.5.2 Whole heart electrophysiology

To model the electrophysiology activity in the cardiac tissue we used the monodomain equation endowed with the TTP and CRN ionic models for the ventricles and for the atria, respectively, with the settings described in Section 5.1.

The interactions among atria and ventricles are based on the following assumptions on the cardiac conductions system (CCS) connections, showed in Figure 14(b). The ventricles are electrically isolated from the atria by the atrio-ventricular grooves [116]; the atria are electrically separated by the insulating nature of the atrial septum (dividing RA from LA) apart from muscular continuity at the rim of Fossa Ovalis [65]. The CCS pathway was modelled as a series of spherical delayed stimuli along the heart geometry that mimic the inter-atrial connections, the atrio-ventricular node delay and the main area of ventricles electrical activation: specifically, when the transmembrane potential front reaches these points a stimulus current is triggered, see Figure 14(b).

The CCS electric signal originates at the Sino-Atrial Node (SAN, $t = 0$ ms) and travels from RA to LA through three inter-atrial connections, the Bach-

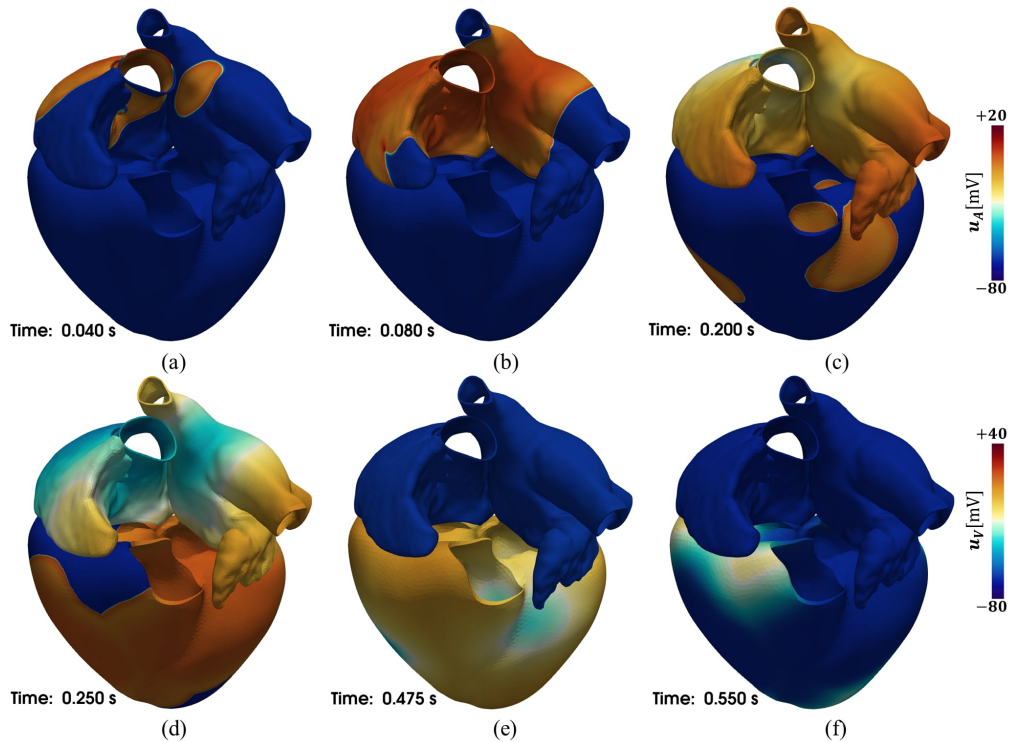


Figure 15: Evolution of the transmembrane potentials for the ventricles u_V and for the atria u_A in the Zygote heart model during a cardiac cycle.

mann’s Bundle (BB, $t = 28$ ms), the rim of Fossa Ovalis (FO, $t = 42$ ms) and the Coronary Sinus Musculature (CSM, $t = 80$ ms) [65, 115]. When the electric signal reaches the Atrio-Ventricular Node (AVN), located at the lower back section of the inter-atrial septum near the coronary sinus opening, it is subject to a delay (90 ms) that allows the complete activation of the atria before ventricles electric propagation starts [65]. Finally, ventricle endocardial areas are activated: in the anterior para-septal wall (AL), in the left surface of inter-ventricular septum (SL) and in the bottom of postero-basal area (PL), for the left ventricle ($t = 160$ ms); in the septum (SR) and in the free endocardial wall (ER), for the right ventricle ($t = 165$ ms) [117].

Figure 14(c) depicts the activation maps computed by the heart electrophysiology simulation. We obtained a physiologically compatible timing for the heart activation [46, 75, 76]: the complete atria depolarization occurs after about 120 ms, while that of ventricles after about $t = 270$ ms. The last region to be activated is LAA for the atria, while the postero-basal area of the right ventricle for the ventricles, both in accordance with [115, 117].

The transmembrane potentials evolution for the ventricles u_V and for the atria u_A are shown in Figure 15. As expected, the electric signal initiates at the SAN and spreads from right to left atrium, see Figures 15(a) and 15(b). Then,

after the delay at the AVN, the ventricles start to activate, see Figure 15(c). The atria repolarization arises during ventricles depolarization, see Figures 15(c-e). Finally, after the isoelectric ventricles activity, the whole heart return to the depolarized initial configuration, see Figure 15(f).

6 Conclusions

In this work, we provided a unified framework for generating cardiac muscle fibers in a full heart computational domain. This allowed us to obtain physically meaningful electrophysiology simulations of a four chambers heart realistic domain.

We first reviewed three existing LDRBMs for fibers generation in the ventricles (R-RBM, B-RBM, D-RBM), by means of a unified description. We proposed some extensions that allow to include different fiber orientations for left and right ventricle for R-RBM and B-RBM, the rotation of all the myofibers vectors for R-RBM and fibers generation up to cardiac valve rings for B-RBM. By comparing the three methods, we found that most of the differences are in the right ventricle endocardium, in the septum, in the inter-ventricular junctions and in the region between the valve rings. We also performed electrophysiology simulations which highlighted that most of the differences occur at the septum, particularly in that part facing the right endocardium. This proved the importance to include a different fiber orientation in the right ventricle with respect to the left one.

We proposed a novel LDRBM to be used for generating atrial fibers and we applied it to both idealized and realistic geometries showing that the atrial LDRBM capture the complex arrangement of fiber directions in almost all the anatomical atrial regions. We analysed the influence of atria fiber bundles by means of electrophysiological simulations in a realistic geometry, verifying the strong effect of their complex architecture in the electric signal propagation.

Finally, we presented an electrophysiology simulation of a realistic four chamber heart including fibers generated by LDRBMs for both atria and ventricles.

We remark that the proposed novel fibers generation methodology, based on LDRBMs, is computationally inexpensive, efficient and easy to implement; moreover, it allows to include realistic cardiac muscle fibers architecture on whole heart geometries of arbitrary shape. As a consequence, it is possible to generate patient cohorts heart fibers, fed by input parameters inferred from histology or DTI studies, through an automated and computationally efficient pipeline. We consider the proposed methodology as an important contribution to incorporate patient specific whole heart fiber field into electrophysiology and electromechanics simulations, aimed both to study clinical cases and to investigate medical questions.

Acknowledgements

This project has received funding from the European Research Council (ERC) under the European Union’s Horizon 2020 research and innovation programme (grant agreement No 740132, iHEART - An Integrated Heart Model for the simulation of the cardiac function, P.I. Prof. A. Quarteroni).



References

- [1] D. D. Streeter Jr, H. M. Spotnitz, D. P. Patel, J. Ross Jr, and E. H. Sonnenblick. Fiber orientation in the canine left ventricle during diastole and systole. *Circulation Research*, 24(3):339–347, 1969.
- [2] D. E. Roberts, L. T. Hersh, and A. M. Scher. Influence of cardiac fiber orientation on wavefront voltage, conduction velocity, and tissue resistivity in the dog. *Circulation Research*, 44(5):701–712, 1979.
- [3] B.B. Punske, B. Taccardi, B. Steadman, P.R. Ershler, A. England, M.L. Valencik, J.A. McDonald, and S.E. Litwin. Effect of fiber orientation on propagation: electrical mapping of genetically altered mouse hearts. *Journal of Electrocardiology*, 38(4):40–44, 2005.
- [4] R. Beyar and S. Sideman. A computer study of the left ventricular performance based on fiber structure, sarcomere dynamics, and transmural electrical propagation velocity. *Circulation Research*, 55(3):358–375, 1984.
- [5] J.D. Bayer, J. Beaumont, and A. Krol. Laplace–Dirichlet energy field specification for deformable models. An FEM approach to active contour fitting. *Annals of Biomedical Engineering*, 33(9):1175–1186, 2005.
- [6] E.W. Hsu, A.L. Muzikant, S.A. Matulevicius, R.C. Penland, and C.S. Henriquez. Magnetic resonance myocardial fiber-orientation mapping with direct histological correlation. *American Journal of Physiology-Heart and Circulatory Physiology*, 274(5):H1627–H1634, 1998.
- [7] P.A. Helm, H.J. Tseng, L. Younes, E.R. McVeigh, and R.L. Winslow. Ex vivo 3D diffusion tensor imaging and quantification of cardiac laminar structure. *Magnetic Resonance in Medicine: An Official Journal of the International Society for Magnetic Resonance in Medicine*, 54(4):850–859, 2005.

- [8] F. Pashakhanloo, D.A. Herzka, H. Ashikaga, S. Mori, N. Gai, D.A. Bluemke, N. Trayanova, and E.R. McVeigh. Myofiber architecture of the human atria as revealed by submillimeter diffusion tensor imaging. *Circulation: Arrhythmia and Electrophysiology*, 9:e004133, 2016.
- [9] D.F. Scollan, A. Holmes, J. Zhang, and R.L. Winslow. Reconstruction of cardiac ventricular geometry and fiber orientation using magnetic resonance imaging. *Annals of Biomedical Engineering*, 28(8):934–944, 2000.
- [10] E.X. Wu, Y. Wu, H. Tang, J. Wang, J. Yang, M.C. Ng, E.S. Yang, C.W. Chan, S. Zhu, C. Lau, et al. Study of myocardial fiber pathway using magnetic resonance diffusion tensor imaging. *Magnetic Resonance Imaging*, 25(7):1048–1057, 2007.
- [11] J.M. Peyrat, M. Sermesant, X. Pennec, H. Delingette, C. Xu, E.R. McVeigh, and N. Ayache. A computational framework for the statistical analysis of cardiac diffusion tensors: application to a small database of canine hearts. *IEEE Transactions on Medical Imaging*, 26(11):1500–1514, 2007.
- [12] H. Lombaert, J. Peyrat, P. Croisille, S. Rapacchi, L. Fanton, F. Chieriet, P. Clarysse, I. Magnin, H. Delingette, and N. Ayache. Human atlas of the cardiac fiber architecture: study on a healthy population. *IEEE Transactions on Medical Imaging*, 31(7):1436–1447, 2012.
- [13] N. Toussaint, C.T. Stoeck, T. Schaeffter, S. Kozerke, M. Sermesant, and P.G. Batchelor. In vivo human cardiac fibre architecture estimation using shape-based diffusion tensor processing. *Medical Image Analysis*, 17(8):1243–1255, 2013.
- [14] A.L. Alexander, K.M. Hasan, M. Lazar, J.S. Tsuruda, and D.L. Parker. Analysis of partial volume effects in diffusion-tensor MRI. *Magnetic Resonance in Medicine: An Official Journal of the International Society for Magnetic Resonance in Medicine*, 45(5):770–780, 2001.
- [15] A. Nagler, C. Bertoglio, M. Gee, and W. Wall. Personalization of cardiac fiber orientations from image data using the unscented Kalman filter. In *International Conference on Functional Imaging and Modeling of the Heart*, pages 132–140, 2013.
- [16] J.M. Hoermann, M.R. Pfaller, L. Avena, C. Bertoglio, and W.A. Wall. Automatic mapping of atrial fiber orientations for patient-specific modeling of cardiac electromechanics using image registration. *International Journal for Numerical Methods in Biomedical Engineering*, 35(6):e3190, 2019.

- [17] J.D. Bayer, R.C. Blake, G. Plank, and N. Trayanova. A novel rule-based algorithm for assigning myocardial fiber orientation to computational heart models. *Annals of Biomedical Engineering*, 40(10):2243–2254, 2012.
- [18] J. Wong and E. Kuhl. Generating fibre orientation maps in human heart models using Poisson interpolation. *Computer Methods in Biomechanics and Biomedical Engineering*, 17(11):1217–1226, 2014.
- [19] S. Rossi, T. Lassila, R. Ruiz-Baier, A. Sequeira, and A. Quarteroni. Thermodynamically consistent orthotropic activation model capturing ventricular systolic wall thickening in cardiac electromechanics. *European Journal of Mechanics-A/Solids*, 48:129–142, 2014.
- [20] R. Doste, D. Soto-Iglesias, G. Bernardino, A. Alcaine, R. Sebastian, S. Giffard-Roisin, M. Sermesant, A. Berruezo, D. Sanchez-Quintana, and O. Camara. A rule-based method to model myocardial fiber orientation in cardiac biventricular geometries with outflow tracts. *International Journal for Numerical Methods in Biomedical Engineering*, 35(4):e3185, 2019.
- [21] M.W. Krueger, V. Schmidt, C. Tobón, F.M. Weber, C. Lorenz, D.U.J. Keller, H. Barschdorf, M. Burdumy, P. Neher, G. Plank, et al. Modeling atrial fiber orientation in patient-specific geometries: a semi-automatic rule-based approach. In *International Conference on Functional Imaging and Modeling of the Heart*, pages 223–232, 2011.
- [22] C. Tobón, C.A. Ruiz-Villa, E. Heidenreich, L. Romero, F. Hornero, and J. Saiz. A three-dimensional human atrial model with fiber orientation. Electrograms and arrhythmic activation patterns relationship. *PloS One*, 8, 2013.
- [23] T.E. Fastl, C. Tobon-Gomez, A. Crozier, J. Whitaker, R. Rajani, K.P. McCarthy, D. Sanchez-Quintana, S.Y. Ho, M.D. O’Neill, G. Plank, et al. Personalized computational modeling of left atrial geometry and transmural myofiber architecture. *Medical Image Analysis*, 2018.
- [24] M. Potse, B. Dubé, J. Richer, A. Vinet, and R. M. Gulrajani. A comparison of monodomain and bidomain reaction-diffusion models for action potential propagation in the human heart. *IEEE Transactions on Biomedical Engineering*, 53(12):2425–2435, 2006.
- [25] P. Nielsen, I.J. Le Grice, B.H. Smaill, and P.J. Hunter. Mathematical model of geometry and fibrous structure of the heart. *American Journal of Physiology-Heart and Circulatory Physiology*, 260(4):H1365–H1378, 1991.
- [26] M. J. Bishop, G. Plank, R.A.B. Burton, J.E. Schneider, D.J. Gavaghan, V. Grau, and P. Kohl. Development of an anatomically detailed MRI-derived rabbit ventricular model and assessment of its impact on simu-

- lations of electrophysiological function. *American Journal of Physiology-Heart and Circulatory Physiology*, 298(2):H699–H718, 2009.
- [27] A. Ferrer, R. Sebastián, D. Sánchez-Quintana, J.F. Rodríguez, E.J. Godoy, L. Martínez, and J. Saiz. Detailed anatomical and electrophysiological models of human atria and torso for the simulation of atrial activation. *PloS One*, 10(11):e0141573, 2015.
- [28] G. Plank, A. Prassl, E. Hofer, and N. Trayanova. Evaluating intramural virtual electrodes in the myocardial wedge preparation: simulations of experimental conditions. *Biophysical Journal*, 94:1904–1915, 2008.
- [29] R.A. Greenbaum, S.Y. Ho, D.G. Gibson, A.E. Becker, and R.H. Anderson. Left ventricular fibre architecture in man. *Heart*, 45(3):248–263, 1981.
- [30] D. Sanchez-Quintana, V. Garcia-Martinez, and J.M. Hurle. Myocardial fiber architecture in the human heart. *Cells Tissues Organs*, 138(4):352–358, 1990.
- [31] R.H. Anderson, M. Smerup, D. Sanchez-Quintana, M. Loukas, and P.P. Lunkenheimer. The three-dimensional arrangement of the myocytes in the ventricular walls. *Clinical Anatomy: The Official Journal of the American Association of Clinical Anatomists and the British Association of Clinical Anatomists*, 22(1):64–76, 2009.
- [32] M.J. Kocica, A.F. Corno, F. Carreras-Costa, M. Ballester-Rodes, M.C. Moghbel, C.N.C. Cueva, V. Lackovic, V.I. Kanjuh, and F. Torrent-Guasp. The helical ventricular myocardial band: global, three-dimensional, functional architecture of the ventricular myocardium. *European Journal of Cardio-thoracic Surgery*, 29:S21–S40, 2006.
- [33] P. Boettler, P. Claus, L. Herbots, M. McLaughlin, J. D’hooge, B. Bijmens, S.Y. Ho, D. Kececioglu, and G.R. Sutherland. New aspects of the ventricular septum and its function: an echocardiographic study. *Heart*, 91(10):1343–1348, 2005.
- [34] M.W. Krueger, K. Rhode, F.M. Weber, D. Keller, D. Caulfield, G. Seemann, B. Knowles, R. Razavi, and O. Dössel. Patient-specific volumetric atrial models with electrophysiological components: a comparison of simulations and measurements. *Biomedizinische Technik/Biomedical Engineering*, 55, 2010.
- [35] S. Labarthe, Y. Coudiere, J. Henry, and H. Cochet. A semi-automatic method to construct atrial fibre structures: A tool for atrial simulations. In *Computing in Cardiology*, pages 881–884, 2012.

- [36] S. Rocher, A. López, A. Ferrer, L. Martínez, D. Sánchez, and J. Saiz. A Highly-Detailed 3D Model of the Human Atria. In *World Congress on Medical Physics and Biomedical Engineering 2018*, pages 649–653. Springer, 2019.
- [37] D.M. Harrild and C.S Henriquez. A computer model of normal conduction in the human atria. *Circulation Research*, 87:e25–e36, 2000.
- [38] E.J. Vigmond, R. Ruckdeschel, and N. Trayanova. Reentry in a morphologically realistic atrial model. *Journal of Cardiovascular Electrophysiology*, 12:1046–1054, 2001.
- [39] V. Jacquemet, N. Virag, Z. Ihara, L. Dang, O. Blanc, S. Zozor, J. Vesin, L. Kappenberger, and C. Henriquez. Study of unipolar electrogram morphology in a computer model of atrial fibrillation. *Journal of Cardiovascular Electrophysiology*, 14:S172–S179, 2003.
- [40] G. Seemann, C. Höper, F.B. Sachse, O. Dössel, A.V. Holden, and H. Zhang. Heterogeneous three-dimensional anatomical and electrophysiological model of human atria. *Philosophical Transactions of the Royal Society A: Mathematical, Physical and Engineering Sciences*, 364:1465–1481, 2006.
- [41] T.E. Fastl, C. Tobon-Gomez, W.A. Crozier, J. Whitaker, R. Rajani, K.P. McCarthy, D. Sanchez-Quintana, S.Y. Ho, M.D. O’Neill, G. Plank, et al. Personalized modeling pipeline for left atrial electromechanics. In *2016 Computing in Cardiology Conference (CinC)*, pages 225–228, 2016.
- [42] N.A. Trayanova. Whole-heart modeling: applications to cardiac electrophysiology and electromechanics. *Circulation Research*, 108:113–128, 2011.
- [43] B. Baillargeon, N. Rebelo, D.D. Fox, R.L. Taylor, and E. Kuhl. The living heart project: a robust and integrative simulator for human heart function. *European Journal of Mechanics-A/Solids*, 48:38–47, 2014.
- [44] T. Fritz, C. Wieners, G. Seemann, H. Steen, and Olaf Dössel. Simulation of the contraction of the ventricles in a human heart model including atria and pericardium. *Biomechanics and Modeling in Mechanobiology*, 13(3):627–641, 2014.
- [45] C.M. Augustin, A. Neic, M. Liebmann, A.J. Prassl, S.A. Niederer, G. Haase, and G. Plank. Anatomically accurate high resolution modeling of human whole heart electromechanics: a strongly scalable algebraic multigrid solver method for nonlinear deformation. *Journal of Computational Physics*, 305:622–646, 2016.

- [46] A. Quarteroni, T. Lassila, S. Rossi, and R. Ruiz-Baier. Integrated Heart—Coupling multiscale and multiphysics models for the simulation of the cardiac function. *Computer Methods in Applied Mechanics and Engineering*, 314:345–407, 2017.
- [47] A. Santiago, J. Aguado-Sierra, M. Zavala-Aké, R. Doste-Beltran, S. Gómez, R. Arís, J.C. Cajas, E. Casoni, and M. Vázquez. Fully coupled fluid-electro-mechanical model of the human heart for supercomputers. *International Journal for Numerical Methods in Biomedical Engineering*, 34(12):e3140, 2018.
- [48] S. Land and S.A. Niederer. Influence of atrial contraction dynamics on cardiac function. *International Journal for Numerical Methods in Biomedical Engineering*, 34(3):e2931, 2018.
- [49] M.R. Pfaller, J.M. Hörmann, M. Weigl, A. Nagler, R. Chabiniok, C. Bertoglio, and W.A. Wall. The importance of the pericardium for cardiac biomechanics: from physiology to computational modeling. *Biomechanics and Modeling in Mechanobiology*, 18(2):503–529, 2019.
- [50] M. Strocchi, M. Gsell, C.M. Augustin, O. Razeghi, C.H. Roney, A.J. Prassl, E.J. Vigmond, J.M. Behar, J.S. Gould, C.A. Rinaldi, et al. Simulating ventricular systolic motion in a four-chamber heart model with spatially varying robin boundary conditions to model the effect of the pericardium. *Journal of Biomechanics*, 101:109645, 2020.
- [51] K. Shoemake. Animating rotation with quaternion curves. In *ACM SIG-GRAPH Computer Graphics*, volume 19, pages 245–254, 1985.
- [52] J.B. Kuipers et al. *Quaternions and Rotation Sequences*, volume 66. Princeton University Press, 1999.
- [53] S.Y. Ho and P. Nihoyannopoulos. Anatomy, echocardiography, and normal right ventricular dimensions. *Heart*, 92:i2–i13, 2006.
- [54] D. Sánchez-Quintana, M. Doblado-Calatrava, J.A. Cabrera, Y. Macías, and F. Saremi. Anatomical basis for the cardiac interventional electrophysiologist. *BioMed Research International*, 2015.
- [55] J. Bayer, A.J. Prassl, A. Pashaei, J.F. Gomez, A. Frontera, A. Neic, G. Plank, and E.J. Vigmond. Universal ventricular coordinates: A generic framework for describing position within the heart and transferring data. *Medical Image Analysis*, 45:83–93, 2018.
- [56] O. Dössel, M.W. Krueger, F.M. Weber, M. Wilhelms, and G. Seemann. Computational modeling of the human atrial anatomy and electrophysiology. *Medical & Biological Engineering & Computing*, 50:773–799, 2012.

- [57] J.P. Boineau, T.E. Canavan, R.B. Schuessler, M.E. Cain, P.B. Corr, and J.L. Cox. Demonstration of a widely distributed atrial pacemaker complex in the human heart. *Circulation*, 77:1221–1237, 1988.
- [58] T.R. Betts, S. Y. Ho, D. Sánchez-Quintana, P.R. Roberts, R.H. Anderson, and J.M. Morgan. Three-dimensional mapping of right atrial activation during sinus rhythm and its relationship to endocardial architecture. *Journal of Cardiovascular Electrophysiology*, 13:1152–1159, 2002.
- [59] R. De Ponti, S.Y. Ho, J.A. Salerno-Uriarte, M. Tritto, and G. Spadacini. Electroanatomic analysis of sinus impulse propagation in normal human atria. *Journal of Cardiovascular Electrophysiology*, 13:1–10, 2002.
- [60] M.W. Krueger. *Personalized multi-scale modeling of the atria: heterogeneities, fiber architecture, hemodialysis and ablation therapy*, volume 19. KIT Scientific Publishing, 2013.
- [61] B. Maesen, S. Zeemering, C. Afonso, J. Eckstein, R. Burton, A. Van Hunnik, D.J. Stuckey, D. Tyler, J. Maessen, V. Grau, et al. Rearrangement of atrial bundle architecture and consequent changes in anisotropy of conduction constitute the 3-dimensional substrate for atrial fibrillation. *Circulation: Arrhythmia and Electrophysiology*, 6:967–975, 2013.
- [62] J. W. Papez. Heart musculature of the atria. *American Journal of Anatomy*, 27:255–285, 1920.
- [63] C.E. Thomas. The muscular architecture of the atria of hog and dog hearts. *American Journal of Anatomy*, 104:207–236, 1959.
- [64] S.Y. Ho, R.H. Anderson, and D. Sánchez-Quintana. Atrial structure and fibres: morphologic bases of atrial conduction. *Cardiovascular Research*, 54:325–336, 2002.
- [65] S.Y. Ho and D. Sánchez-Quintana. The importance of atrial structure and fibers. *Clinical Anatomy: The Official Journal of the American Association of Clinical Anatomists and the British Association of Clinical Anatomists*, 22:52–63, 2009.
- [66] S.Y. Ho, J.A. Cabrera, and D. Sanchez-Quintana. Left atrial anatomy revisited. *Circulation: Arrhythmia and Electrophysiology*, 5:220–228, 2012.
- [67] O.V. Aslanidi, T. Nikolaidou, J. Zhao, B.H. Smaill, S. Gilbert, A.V. Holden, T. Lowe, P.J. Withers, R.S. Stephenson, J.C. Jarvis, et al. Application of micro-computed tomography with iodine staining to cardiac imaging, segmentation, and computational model development. *IEEE Transactions on Medical Imaging*, 32:8–17, 2012.

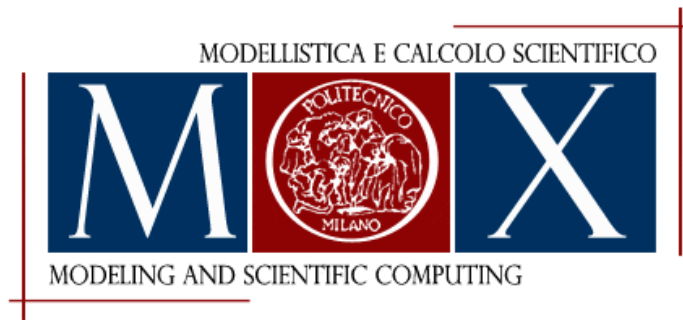
- [68] D. D. Sánchez-Quintana, G. Pizarro, J.R. López-Mínguez, S.Y. Ho, and J.A. Cabrera. Standardized review of atrial anatomy for cardiac electrophysiologists. *Journal of Cardiovascular Translational Research*, 6:124–144, 2013.
- [69] B.J. Hansen, J. Zhao, and V.V. Fedorov. Fibrosis and atrial fibrillation: computerized and optical mapping: a view into the human atria at sub-millimeter resolution. *JACC: Clinical Electrophysiology*, 3:531–546, 2017.
- [70] J. Zhao, B.J. Hansen, T.A. Csepe, P. Lim, Y. Wang, M. Williams, P.J. Mohler, P.M.L. Janssen, R. Weiss, J.D. Hummel, et al. Integration of high-resolution optical mapping and 3-dimensional micro-computed tomographic imaging to resolve the structural basis of atrial conduction in the human heart. *Circulation: Arrhythmia and Electrophysiology*, 8:1514–1517, 2015.
- [71] J. Zhao, B.J. Hansen, Y. Wang, T.A. Csepe, L.V. Sul, A. Tang, Y. Yuan, N. Li, A. Bratasz, K.A. Powell, et al. Three-dimensional integrated functional, structural, and computational mapping to define the structural “fingerprints” of heart-specific atrial fibrillation drivers in human heart ex vivo. *Journal of the American Heart Association*, 6:e005922, 2017.
- [72] A. Satriano, C. Bellini, E.J. Vigmond, and E.S. Di Martino. A feature-based morphing methodology for computationally modeled biological structures applied to left atrial fiber directions. *Journal of Biomechanical Engineering*, 135, 2013.
- [73] K.S. McDowell, S. Zahid, F. Vadakkumpadan, J. Blauer, R.S. MacLeod, and N. Trayanova. Virtual electrophysiological study of atrial fibrillation in fibrotic remodeling. *PloS One*, 10, 2015.
- [74] C.H. Roney, A. Pashaei, M. Meo, R. Dubois, P.M. Boyle, N. Trayanova, H. Cochet, S.A. Niederer, and E.J. Vigmond. Universal atrial coordinates applied to visualisation, registration and construction of patient specific meshes. *Medical Image Analysis*, 55:65–75, 2019.
- [75] P.C. Franzone, L.F. Pavarino, and S. Scacchi. *Mathematical Cardiac Electrophysiology*, volume 13. Springer, 2014.
- [76] A. Quarteroni, L. Dedè, A. Manzoni, and C. Vergara. *Mathematical Modelling of the Human Cardiovascular System: Data, Numerical Approximation, Clinical Applications*. Cambridge University Press, 2019.
- [77] M. Courtemanche, R.J. Ramirez, and S. Nattel. Ionic mechanisms underlying human atrial action potential properties: insights from a mathematical model. *American Journal of Physiology-Heart and Circulatory Physiology*, 275:H301–H321, 1998.

- [78] K.H.W.J. Ten Tusscher and A.V. Panfilov. Alternans and spiral breakup in a human ventricular tissue model. *American Journal of Physiology-Heart and Circulatory Physiology*, 291:H1088–H1100, 2006.
- [79] E.J. Vigmond, M. Hughes, G. Plank, and L.J. Leon. Computational tools for modeling electrical activity in cardiac tissue. *Journal of Electrocardiology*, 36:69–74, 2003.
- [80] G. Plank, L. Zhou, J.L. Greenstein, S. Cortassa, R. L Winslow, B. O’Rourke, and N.A. Trayanova. From mitochondrial ion channels to arrhythmias in the heart: computational techniques to bridge the spatio-temporal scales. *Philosophical Transactions of the Royal Society A: Mathematical, Physical and Engineering Sciences*, 366:3381–3409, 2008.
- [81] N.A. Trayanova, P.M. Boyle, H.J. Arevalo, and S. Zahid. Exploring susceptibility to atrial and ventricular arrhythmias resulting from remodeling of the passive electrical properties in the heart: a simulation approach. *Frontiers in Physiology*, 5:435, 2014.
- [82] S.A. Niederer, J. Lumens, and N.A. Trayanova. Computational models in cardiology. *Nature Reviews Cardiology*, 16:100–111, 2019.
- [83] E.J. Vigmond, R.W. Dos Santos, A.J. Prassl, M. Deo, and G. Plank. Solvers for the cardiac bidomain equations. *Progress in Biophysics and Molecular Biology*, 96:3–18, 2008.
- [84] S. Krishnamoorthi, M. Sarkar, and W.S. Klug. Numerical quadrature and operator splitting in finite element methods for cardiac electrophysiology. *International Journal for Numerical Methods in Biomedical Engineering*, 29:1243–1266, 2013.
- [85] Y. Saad and M.H. Schultz. GMRES: A generalized minimal residual algorithm for solving nonsymmetric linear systems. *SIAM Journal on Scientific and Statistical Computing*, 7:856–869, 1986.
- [86] Zygote Media Group Inc. Zygote solid 3d heart generation II development report. *Technical report*, 2014.
- [87] M. Sermesant, K. Rhode, G.I. Sanchez-Ortiz, O. Camara, R. Andriantsimivavona, S. Hegde, D. Rueckert, P. Lambiase, C. Bucknall, E. Rosenthal, et al. Simulation of cardiac pathologies using an electromechanical biventricular model and XMR interventional imaging. *Medical Image Analysis*, 9(5):467–480, 2005.
- [88] L. Pegolotti, L. Dedè, and A. Quarteroni. Isogeometric Analysis of the electrophysiology in the human heart: Numerical simulation of the bidomain equations on the atria. *Computer Methods in Applied Mechanics and Engineering*, 343:52–73, 2019.

- [89] L. Antiga and D.A. Steinman. The vascular modeling toolkit. *URL: <http://www.vmtk.org>*, 2008.
- [90] M. Fedele. Polygonal surface processing and mesh generation tools for numerical simulations of the complete cardiac function. *MOX Report 32*, Politecnico di Milano, 2019.
- [91] D. Arndt, W. Bangerth, T.C. Clevenger, D. Davydov, M. Fehling, D. Garcia-Sanchez, G. Harper, T. Heister, L. Heltai, M. Kronbichler, R.M. Kynch, M. Maier, J.-P. Pelteret, B. Turcksin, and D. Wells. The deal.II Library, Version 9.1. *Journal of Numerical Mathematics*, 2019.
- [92] B.J. Roth. Action potential propagation in a thick strand of cardiac muscle. *Circulation Research*, 68:162–173, 1991.
- [93] S.A. Niederer, E. Kerfoot, A.P. Benson, M.O. Bernabeu, O. Bernus, C. Bradley, E.M. Cherry, R. Clayton, F.H. Fenton, A. Garny, et al. Verification of cardiac tissue electrophysiology simulators using an N-version benchmark. *Philosophical Transactions of the Royal Society A: Mathematical, Physical and Engineering Sciences*, 369:4331–4351, 2011.
- [94] C.M. Costa, E. Hoetzel, B.M. Rocha, A.J. Prassl, and G. Plank. Automatic parameterization strategy for cardiac electrophysiology simulations. In *Computing in Cardiology*, pages 373–376, 2013.
- [95] L. Clerc. Directional differences of impulse spread in trabecular muscle from mammalian heart. *The Journal of Physiology*, 255:335–346, 1976.
- [96] D.E. Roberts and A.M. Scher. Effect of tissue anisotropy on extracellular potential fields in canine myocardium in situ. *Circulation Research*, 50:342–351, 1982.
- [97] C.W. Zemlin, H. Herzel, S.Y. Ho, and A. Panfilov. A realistic and efficient model of excitation propagation in the human atria. *Computer Simulation and Experimental Assessment of Cardiac Electrophysiology*, pages 29–34, 2001.
- [98] D.A. Hooks, M.L. Trew, B.J. Caldwell, G.B. Sands, I.J. LeGrice, and B.H. Smaill. Laminar arrangement of ventricular myocytes influences electrical behavior of the heart. *Circulation Research*, 101:e103–e112, 2007.
- [99] H. Dimitri, M. Ng, A.G. Brooks, P. Kuklik, M.K. Stiles, D.H. Lau, N. Antic, A. Thornton, D.A. Saint, D. McEvoy, et al. Atrial remodeling in obstructive sleep apnea: implications for atrial fibrillation. *Heart Rhythm*, 9:321–327, 2012.
- [100] A. Lopez-Perez, R. Sebastian, and J.M. Ferrero. Three-dimensional cardiac computational modelling: methods, features and applications. *Biomedical Engineering Online*, 14:35, 2015.

- [101] D.E. Hurtado and G. Rojas. Non-conforming finite-element formulation for cardiac electrophysiology: an effective approach to reduce the computation time of heart simulations without compromising accuracy. *Computational Mechanics*, 61(4):485–497, 2018.
- [102] J. Jilberto and D.E. Hurtado. Semi-implicit non-conforming finite-element schemes for cardiac electrophysiology: a framework for mesh-coarsening heart simulations. *Frontiers in Physiology*, 9:1513, 2018.
- [103] H.J. Arevalo, F. Vadakkumpadan, E. Guallar, A. Jebb, P. Malamas, K.C. Wu, and N.A. Trayanova. Arrhythmia risk stratification of patients after myocardial infarction using personalized heart models. *Nature Communications*, 7:1–8, 2016.
- [104] A.A. Razumov, K.S. Ushenin, K.A. Butova, and O.E. Solovyova. The study of the influence of heart ventricular wall thickness on pseudo-ECG. *Russian Journal of Numerical Analysis and Mathematical Modelling*, 33:301–313, 2018.
- [105] S. Göktepe, J. Wong, and E. Kuhl. Atrial and ventricular fibrillation: computational simulation of spiral waves in cardiac tissue. *Archive of Applied Mechanics*, 80(5):569–580, 2010.
- [106] S. Göktepe and E. Kuhl. Electromechanics of the heart: a unified approach to the strongly coupled excitation–contraction problem. *Computational Mechanics*, 45(2-3):227–243, 2010.
- [107] A. Ahmad Bakir, A. Al Abed, M.C. Stevens, N.H. Lovell, and S. Dokos. A Multiphysics Biventricular Cardiac Model: Simulations With a Left-Ventricular Assist Device. *Frontiers in Physiology*, 9:1259, 2018.
- [108] J.C. Mercier, T.G. DiSessa, J.M. Jarmakani, T. Nakanishi, S. Hiraishi, J. Isabel-Jones, and W.F. Friedman. Two-dimensional echocardiographic assessment of left ventricular volumes and ejection fraction in children. *Circulation*, 65:962–969, 1982.
- [109] P.P. Lunkenheimer, P. Niederer, D. Sanchez-Quintana, M. Murillo, and M. Smerup. Models of ventricular structure and function reviewed for clinical cardiologists. *Journal of Cardiovascular Translational Research*, 6:176–186, 2013.
- [110] R.S. Stephenson, P. Agger, P.P. Lunkenheimer, J. Zhao, M. Smerup, P. Niederer, R.H. Anderson, and J.C. Jarvis. The functional architecture of skeletal compared to cardiac musculature: Myocyte orientation, lamellar unit morphology, and the helical ventricular myocardial band. *Clinical Anatomy*, 29:316–332, 2016.

- [111] A.S. Patelli, L. Dedè, T. Lassila, A. Bartzzaghi, and A. Quarteroni. Iso-geometric approximation of cardiac electrophysiology models on surfaces: An accuracy study with application to the human left atrium. *Computer Methods in Applied Mechanics and Engineering*, 317:248–273, 2017.
- [112] R. Beinart, S. Abbara, A. Blum, M. Ferencik, K. Heist, J. Ruskin, and M. Mansour. Left atrial wall thickness variability measured by CT scans in patients undergoing pulmonary vein isolation. *Journal of Cardiovascular Electrophysiology*, 22(11):1232–1236, 2011.
- [113] A. Goette, J.M. Kalman, L. Aguinaga, J. Akar, J.A. Cabrera, S.A. Chen, S.S. Chugh, D. Corradi, A. D’Avila, D. Dobrev, et al. EHRA/HRS/APHRS/SOLAECE expert consensus on atrial cardiomyopathies: definition, characterization, and clinical implication. *Ep Europace*, 18(10):1455–1490, 2016.
- [114] J. Saiz and C. Tobón. Supraventricular arrhythmias in a realistic 3d model of the human atria. In *Cardiac Electrophysiology: From Cell to Bedside*, pages 351–359. 2014.
- [115] S.I. Sakamoto, T. Nitta, Y. Ishii, Y. Miyagi, H. Ohmori, and K. Shimizu. Interatrial electrical connections: the precise location and preferential conduction. *Journal of Cardiovascular Electrophysiology*, 16(10):1077–1086, 2005.
- [116] R.H. Anderson, S.Y. Ho, and A.E. Becker. Anatomy of the human atrio-ventricular junctions revisited. *The Anatomical Record: An Official Publication of the American Association of Anatomists*, 260(1):81–91, 2000.
- [117] D. Durrer, R.Th. Van Dam, G.E. Freud, M.J. Janse, F.L. Meijler, and R.C. Arzbaecher. Total excitation of the isolated human heart. *Circulation*, 41(6):899–912, 1970.



MOX-Report No. 29/2020

**Modeling cardiac muscle fibers in ventricular and atrial
electrophysiology simulations**

Piersanti, R.; Africa, P.C.; Fedele, M.; Vergara, C.; Dede', L.;
Corno, A.F.; Quarteroni, A.

MOX, Dipartimento di Matematica
Politecnico di Milano, Via Bonardi 9 - 20133 Milano (Italy)

mox-dmat@polimi.it

<http://mox.polimi.it>